

# Thermo-hydro-mechanical response of a large piled raft equipped with energy piles: a parametric study

Diana Salciarini<sup>1</sup>  · Federica Ronchi<sup>1</sup> · Claudio Tamagnini<sup>1</sup>

Received: 12 October 2016 / Accepted: 6 April 2017 / Published online: 24 April 2017  
© Springer-Verlag Berlin Heidelberg 2017

**Abstract** This paper presents the results of a parametric study in which a series of fully coupled, 3-dimensional thermo-hydro-mechanical Finite Element (FE) analyses has been conducted to investigate the effects of the thermal changes imposed by the regular performance of a GSHP system driven by energy piles on a very large piled raft. The FE simulation program has been focused mainly on the evaluation of the following crucial aspects of the energy system design: the assessment of the soil–pile–raft interaction effects during thermal loading conditions; the quantification of the influence of the thermal properties of the soil and of the geometrical layout of the energy piles on the soil–foundation system response, and the evaluation of the influence of the active pile spacing on the thermal performance of the GSHP–energy pile system. The results of the numerical simulations show that the soil–pile–raft interaction effects can be very important. In particular, the presence of a relatively rigid raft in direct contact with the soil is responsible for axial load variations in inactive piles of the same order of those experienced by the thermo-active piles, even when the latter are relatively far and temperature changes in inactive piles are small. As far as the effect of pile spacing is concerned, the numerical simulations show that placing a high number of energy

piles in a large piled raft with relatively small pile spacings can lead to a significant reduction of the overall heat exchange from the piles to the soil, thus reducing the thermal efficiency of the system.

**Keywords** Energy piles · Finite element modeling · Geothermal energy · Thermo-hydro-mechanical soil–structure interaction

## 1 Introduction

In the last decades, the need of finding renewable and alternative energy sources for providing environmentally-friendly heating, ventilation and air conditioning (HVAC) systems for buildings that limit the production of CO<sub>2</sub>, has led to a considerable increase in the use of ground source heat pumps (GSHPs) connected to foundation structures—often referred to as “energy foundations” or “thermo-active ground structures” [9, 22, 24]. The basic feature of these innovative energy systems is the possibility of exploiting the foundation of the building, already required for structural reasons, as a heat exchanger to remove heat from the building and store it in the ground during summer, or to extract heat from the ground during winter to heat the building. This is achieved by circulating a heat carrier fluid (i.e., water, saline solutions or water–glycol mixtures) in the pipes of the primary circuit of a traditional GSHP system, properly located within the foundation, see, e.g., [1, 9]. The advantages in terms of system efficiency, energy saving and minimum environmental impact have allowed to quickly reach a wide diffusion of energy foundation technology, particularly in Northern European countries (Sweden, Germany, France, Switzerland and Austria), see [16].

✉ Diana Salciarini  
diana.salciarini@unipg.it

Federica Ronchi  
federica.ronchi@strutture.unipg.it

Claudio Tamagnini  
claudio.tamagnini@unipg.it

<sup>1</sup> Department of Civil and Environmental Engineering,  
University of Perugia, Via G. Duranti 93, 06125 Perugia,  
Italy

While the technological aspects of GSHP systems employing energy piles are now fairly well understood, a significant research effort has recently been devoted to the investigation of the thermo-mechanical effects induced in both the foundation structures and the soil by the temperature variations imposed by the GSHP system, particularly in terms of thermo-induced stresses and displacements on piles and pore water pressure variations in relatively low permeability soils.

Experimental investigations on this topic include a number of full-scale in-situ tests on energy piles, as well as tests on small-scale models under artificial gravity. The first in-situ test on an energy pile prototype built as a part of the piled foundation of a building at the Swiss Federal Institute of Technology in Lausanne (EPFL), under actual working conditions, has been reported by Laloui et al. [25]. Bourne-Webb et al. [7] conducted a constant load, cyclic thermal test on a heavily instrumented test pile in London clay. Akrouch et al. [2] investigated the response of a thermo-mechanical (TM) tension load test on an energy pile in high plasticity stiff clays. Murphy et al. [30] conducted a series of thermal response tests on eight full-scale energy foundations in coarse-grained soils, with various heat exchanger configurations. Murphy and McCartney [29] report data from two full-scale energy foundations beneath an 8-story building for a very long observation period (658 days). Stewart and McCartney [36] used centrifuge modeling to obtain experimental data from a heavily instrumented small-scale end bearing energy pile immersed in a unsaturated silt, under carefully controlled environmental conditions. Goode and McCartney [17] also used small-scale centrifuge tests to investigate the effects of end restraints on soil–structure interaction in energy piles in dry sand and unsaturated silt. The interaction effects within a group of energy piles were investigated by Mimouni and Laloui [27] through full-scale in situ experiments on a foundation of four energy piles. Rotta Loria and Laloui [34] analyzed the thermally induced “group effects” among closely spaced energy piles by means of full-scale in situ test and coupled 3-dimensional (3D) TM FE analyses. You et al. [40] conducted full-scale field tests on “Cement Fly-ash Gravel (CFG) energy piles” to study their thermo-mechanical behavior. Ng et al. [31] investigated the effects of cyclic heating and cooling between 9 and 38 °C on the long-term displacement of an energy pile in lightly overconsolidated and heavily overconsolidated kaolin clay through centrifuge modeling.

In parallel with experimental investigations, numerical simulations on the response of single energy piles have been conducted in the attempt of interpreting the complex soil–pile–structure interaction processes activated by the time-dependent temperature changes. Laloui et al. [25] performed a fully coupled thermo-hydro-mechanical

(THM) FE analysis of the test pile in the experimental facility at EPFL using a thermoelastic perfectly plastic Drucker–Prager model for the soils. Wang et al. [38] used a similar approach to model a small-scale centrifuge test, adopting a linear thermoelastic model for the soil. More recently, Wang et al. [39] extended their previous work to take into account the partial saturation of the soil and nonlinear behavior of the soil, modeled with an isotropic hardening Modified Cam–Clay model with thermal softening. Olgun et al. [33] studied the long-term performance of energy piles and their efficiency as heat exchangers in regions where the energy demand is non-symmetrical. A 3D parametric study to investigate the effects of different pipe configurations, pile slenderness and imposed flow rates of the heat carrier fluid on a single energy pile has been presented by Batini et al. [5].

As far as pile groups behavior is concerned, a series of 3D thermoelastic FE analyses have been performed by Salciarini et al. [35] to investigate the mechanical and thermal interaction effects induced in a small circular piled raft in a coarse-grained, high-permeability soil. A fully coupled THM FE simulation has been carried out by Di Donna and Laloui [14] to investigate the pile and soil response in a  $3 \times 7$  rectangular piled raft in clay during several operation cycles (for a period of 10 years), adopting the advanced thermo-elastoplastic model ACMEG–T for the fine-grained soil. Jeong et al. [21] studied the thermo-mechanical behavior of energy piles in a pile group by coupled multi-physical 3D FE analyses with varying pile spacing, pile arrangement, soil type, and end bearing condition. Numerical analyses including a comparison between a single energy pile and an energy pile group with different boundary conditions at the pile head were conducted by Suryatriyastuti et al. [37] with the aim of studying the long-term cyclic interaction mechanism in the group. Di Donna et al. [15] conducted a 3D THM FE analyses for investigating the behavior of a group of energy piles for which experimental data were available.

The aim of the present work is to extend the previous works of Salciarini et al. [35] and Di Donna and Laloui [14] to the case of a very large piled raft in stiff clayey soils. To this end, a series of 3D fully coupled THM FE simulations has been performed, considering a representative “elementary cell” of the foundation. The FE simulation program focused mainly on evaluating the following crucial aspects of the energy foundation design: (a) the assessment of the soil–pile–raft interaction effects during thermal loading conditions; (b) the quantification of the influence of the thermal soil property variability and of the geometrical layout of the energy piles on the soil–foundation system response; and, (c) the influence of the distance among thermo-active piles on the thermal performance of the GSHP–energy pile system.

The paper is organized as follows. The geometry of the ideal—yet realistic—problem considered is detailed in Sect. 2. The mathematical formulation of the coupled THM problem, along with the details of the FE model adopted in the numerical simulations, is provided in Sect. 3. Selected results from the numerical analyses are presented in Sect. 4. First, the soil–foundation response upon thermal loading conditions is discussed in detail for a reference case. Then, the results of a series of parametric studies are presented to assess the influence of such important thermal properties of the soil as the thermal expansion coefficient and the thermal conductivity, as well as of the adopted energy pile layout, on the overall soil–foundation system performance. Concluding remarks and suggestions for further studies are given in Sect. 5.

*Notation* In the following, direct tensor notation is used, with vectors and tensors represented with boldface letters. The symbol “ $\cdot$ ” is used to denote the scalar product of two

vectors or tensors. The symbol “ $\nabla$ ” is used to denote the gradient of a scalar (as in  $\nabla T$ ) or the divergence of a vector or a tensor (as in  $\nabla \cdot \boldsymbol{\nu}$  or  $\nabla \cdot \boldsymbol{\sigma}$ ). Solid mechanics sign convention (traction and extension positive) is adopted for the stresses and strain of the solid skeleton; pore water pressure is assumed positive in compression.

## 2 Problem geometry and soil profile

In this work, the piled foundation of a large framed reinforced concrete multi-story building, with a fairly regular disposition of the pillars in plan (on a  $5 \times 5 \text{ m}^2$  grid), has been considered. The foundation structure is a piled raft, with thickness of 0.5 m, on 25 m long drilled piles with a diameter of 0.6 m, regularly spaced at a distance of 2.5 m along the two main axes of the building, see Fig. 1a. Some of the piles—the thermo-active piles—are equipped with

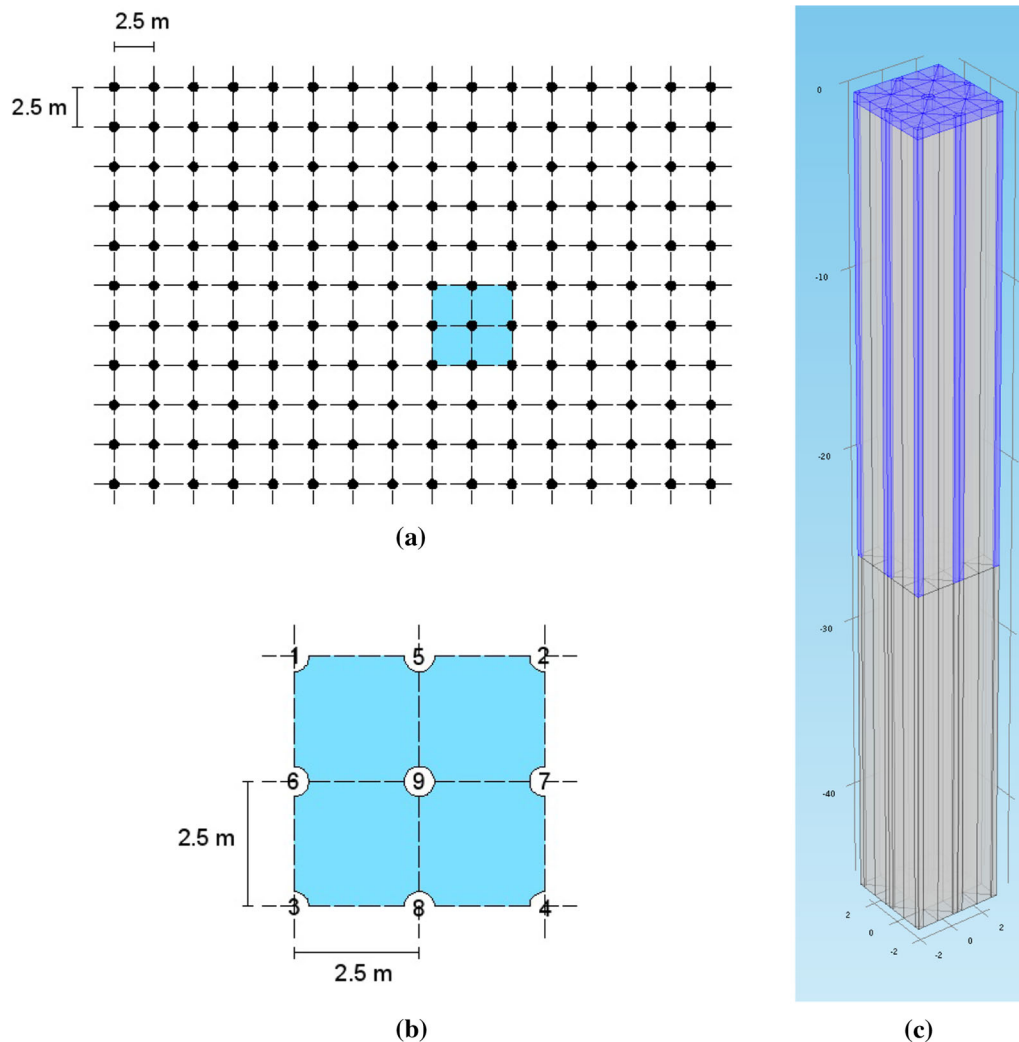


**Fig. 1** Layout of the piled raft considered: **a** plan view with indication of the elementary cell; **b** elementary cell and pile numbering; **c** isometric view of the elementary cell and soil profile

high-density polyethylene (HDPE) pipes to work as energy piles for the GSHP system. The base of the raft is placed at a depth of 0.5 m from the ground surface. Although idealized, this layout is similar to the one employed in several large projects such as the Main Tower building or the PalaisQuartier complex in Frankfurt [23].

Given the assumed symmetry and regularity of the building geometry and external loading conditions, the study has been limited to a single elementary cell of the piled raft (Fig. 1b), which includes a central pile ( $P_9$ ), 4 external half piles on the sides of the cell ( $P_5, P_6, P_7$ , and  $P_8$ ) and 4 angular quarter piles ( $P_1, P_2, P_3$ , and  $P_4$ ) at its vertices. It is worth noting that referring to a unitary cell represents a worst-case scenario for the vertical load variation in the piles.

The soil is a homogeneous, stiff, heavily overconsolidated clay layer extending to a depth of 45.0 m from the base of the raft. The clay layer is underlain by a very stiff and impervious bedrock. The soil is assumed to be fully saturated, with the groundwater table located at the raft base. A 3D view of the foundation geometry and soil profile, limited to the elementary cell under study, is shown in Fig. 1c.

### 3 Coupled THM modeling of the piled raft

#### 3.1 Governing equations and constitutive models adopted

To model the thermo-hydro-mechanical soil–structure interaction effects induced by the operation of the energy piles during heating and cooling stages, a fully coupled THM formulation has been considered. Under the assumption of linear kinematics (“small deformations”) and full saturation of the soils, the balance of mass, momentum and energy equations for the porous medium read [26]:

$$\nabla \cdot \boldsymbol{\sigma}' - \nabla u + \rho \mathbf{b} = \mathbf{0} \quad (1)$$

$$\frac{1}{Q} \dot{u} - \beta_{\text{eff}} \dot{T} + \nabla \cdot \mathbf{v}^s + \nabla \cdot \mathbf{w}^w = 0 \quad (2)$$

$$\rho C_{p,\text{eff}} \dot{T} + \nabla \cdot \mathbf{q} + \rho_w C_{p,w} \mathbf{w}^w \cdot \nabla T = 0 \quad (3)$$

where:  $\boldsymbol{\sigma}' = \boldsymbol{\sigma} + u\mathbf{I}$  is the effective stress tensor;  $u$  is the pore water pressure;  $T$  is the absolute temperature;  $\mathbf{w}^w = n(\mathbf{v}^w - \mathbf{v}^s)$  is the Darcy velocity of the pore water;  $\mathbf{v}^w$  and  $\mathbf{v}^s$  are the velocities of the pore water and the solid skeleton, respectively;  $\mathbf{q}$  is the heat flux vector;  $\mathbf{b}$  is the body force vector (gravity) per unit mass;

$$\frac{1}{Q} = \frac{n}{K_w} + \frac{(1-n)}{K_s}$$

is a storage coefficient accounting for the compressibilities of pore water ( $1/K_w$ ) and solid grains ( $1/K_s$ ), and:

$$\rho := n\rho_w + (1-n)\rho_s$$

$$\beta_{\text{eff}} := n\beta_w + (1-n)\beta_s$$

$$\rho C_{p,w} := (1-n)\rho_s C_{p,s} + n\rho_w C_{p,w}$$

are the average density, thermal expansion coefficient and heat capacity of the porous medium, respectively. These quantities are obtained as volume averages of the densities  $\rho_s$  and  $\rho_w$ , of the thermal expansion coefficients  $\beta_s$  and  $\beta_w$  and of the heat capacities  $\rho_s C_{p,s}$  and  $\rho_w C_{p,w}$  of the solid and liquid phases.

The closure of the governing Eqs. (1)–(3) requires the introduction of suitable constitutive equations for the water flux  $\mathbf{w}^w$ , the heat flux  $\mathbf{q}$  and the effective stress tensor  $\boldsymbol{\sigma}'$ . For the first two quantities, Darcy’s law and Fourier’s law are assumed to be valid:

$$\mathbf{w}^w = \frac{1}{\mu_w} \boldsymbol{\kappa} (-\nabla u + \rho_w \mathbf{b}) \quad (4)$$

$$\mathbf{q} = -\lambda_{\text{eff}} \nabla T \quad (5)$$

where  $\mu_w$  is the dynamic viscosity of the pore water;  $\boldsymbol{\kappa}$  is the intrinsic permeability of the solid skeleton; and

$$\lambda_{\text{eff}} = n\lambda_w + (1-n)\lambda_s$$

is the thermal conductivity of the porous medium, given by the volume average of the thermal conductivities of the solid ( $\lambda_s$ ) and of the liquid ( $\lambda_w$ ) phases. In the following, both thermal conductivities and heat capacities of the two phases are considered independent of temperature.

Both soil and piles have been considered as linear thermoelastic materials where the effective stress reads:

$$\boldsymbol{\sigma}' = \mathbf{D}^e \boldsymbol{\epsilon} - \mathbf{m}^e \dot{T} \quad (6)$$

in which:

$$\mathbf{D}^e = K\mathbf{1} \otimes \mathbf{1} - 2G \left\{ \mathbf{I} - \frac{1}{3} \mathbf{1} \otimes \mathbf{1} \right\} \quad \mathbf{m}^e = \frac{1}{3} K \beta_{\text{eff}} \mathbf{1}$$

are the elastic stiffness tensor and the thermal coupling tensor;  $K$  is the bulk modulus of the solid skeleton;  $G$  is the shear modulus of the solid skeleton, and  $\mathbf{I}$  and  $\mathbf{1}$  are the fourth-order and the second-order unit tensors, respectively.

It is well known that under an increase in temperature in drained conditions, fine-grained soils undergo a permanent change in volume, which is strongly influenced by the overconsolidation ratio, see e.g., [4, 10–12, 24]. In undrained conditions, changes in temperature are accompanied by a permanent pore pressure variation, which in anisotropically normally consolidated soil may eventually lead the material to failure, see, e.g., [20]. Changes in yield stress under both isotropic and deviatoric loading paths are observed under non-isothermal conditions in both soils and rocks. In addition, a clear transition from brittle to ductile

**Table 1** Thermo-hydro-mechanical properties of the clay soil and concrete

	Soil	Concrete
$\gamma$ (kN/m <sup>3</sup> )	20	25
$K$ (MPa)	20	24510
$G$ (MPa)	12	9398
$k$ (m/s)	$10^{-8}$	$10^{-9}$
$\beta_{\text{eff}}$ (1/K)	Variable	$1.0 \times 10^{-5}$
$\lambda_{\text{eff}}$ [W/(mK)]	Variable	1.8
$C_{p,\text{eff}}$ [J/(kgK)]	3034	880

behavior at failure is observed in stiff soils and weak rocks as temperature increases [18, 19]. However, for a stiff OC clay subject to relatively limited temperature changes, the assumption of linear thermoelastic response of the solid skeleton is considered acceptable as a first approximation of the real soil behavior, see for example ref. [38].

The physical and mechanical properties adopted for the stiff clay layer and the reinforced concrete are summarized in Table 1. In the reference simulation, the soil thermal properties—i.e., conductivity  $\lambda_{\text{eff}}$ , heat capacity  $C_{p,\text{eff}}$  and thermal expansion coefficient  $\beta_{\text{eff}}$ —have been set equal to 1.7 W/(mK), 3034 J/(kgK) and  $1.0 \times 10^{-4}$  1/K, respectively, after Ref. [28]. The latter corresponds to a value of the thermal expansion coefficient of the solid grains,  $\beta_s$ , equal to  $3.5 \times 10^{-5}$  1/K. To investigate the influence of  $\lambda_{\text{eff}}$  and  $\beta_{\text{eff}}$  on the soil–foundation response to thermal changes, these two constants have been modified in some of the FE simulations, as reported in the following Sect. 3.3. It is worth noting that all the values adopted for the thermal expansion coefficient of the solid grains,  $\beta_s$ , are much smaller than the thermal expansion coefficient of the pore water,  $\beta_w$ , which in this work has been assumed equal to  $2.1 \times 10^{-4}$  1/K.

### 3.2 Initial and boundary conditions

As for the initial conditions, a geostatic stress state has been imposed to the clay layer, with a coefficient of earth pressure at rest  $K_0 = 0.56$ . The groundwater has been assumed in hydrostatic conditions, with the water table located at a depth of  $z = -0.5$  m (depth of the lower surface of the slab). A constant initial temperature equal to 20 °C has been assumed for the entire domain.

Fixed displacements have been assumed at the base of the soil layer, assumed as perfectly rigid and rough. The normal component of the displacement vector has been fixed on the vertical planes of symmetry. On the top surface of the slab (at  $z = 0$ ), a concentrated vertical downward load of 1500 kN has been applied at the center of the unit cell (on axis of the central pile), to simulate the load

transmitted to the foundation by the superstructure at the base of each column. This load has been applied in drained, isothermal conditions in the first simulation stage, together with the unit weight of the foundation structure.

A no-flow boundary condition has been assumed on the vertical symmetry planes, as well as at the bottom of the clay layer, considering the bedrock as impervious. The pore water pressure  $u$  has been assumed as atmospheric at the raft–soil contact ( $z = -0.5$  m) due to the presence of a thin drainage mat.

A zero heat flux boundary condition has been adopted on the vertical symmetry planes, as well as at the ground surface, considering heat exchanges at the top surface of the slab as negligible. The same assumption has been considered also at the bottom of the clay layer, given that the thermal conductivity of the intact bedrock might be much lower than that of the overlying soil [28]. It is worth noting that, as shown by a few preliminary simulations, this boundary is located deep enough from the pile tip to prevent against possible boundary effects on the thermal system response.

To simulate the normal operation of the GSHP system, in the second (transient) stage of the FE simulations, the temperature of the thermo-active piles (varying in number over the different simulations performed) has been assumed as uniform and varying with time with a sinusoidal pattern as shown in Fig. 2, with a period of 1 year and an amplitude of 20 °C (to ensure a temperature oscillation from 0 to 40 °C). A total simulation time of 2 years (two heating cycles and two cooling cycles) has been considered in this study, to assess the effect of repeated thermal cycles on the response of the soil–foundation system; daily variations of temperature have been ignored.

### 3.3 Finite element discretization and numerical simulation program

The 3D FE model adopted in the simulations—performed with the FE code COMSOL Multiphysics [13]—is shown in Fig. 3. The domain has been discretized with 9570 hexahedral elements with triquadratic interpolation for the displacements and trilinear interpolation for the temperature and the pore water pressure, for a total number of 260,135 degrees of freedom. The pile–soil interface has been considered as perfectly rough (full adhesion), and no soil–pile interface elements have been introduced. The numerical integration in time of the system of ODEs resulting from the spatial discretization of the governing Eqs. (1)–(3) has been carried out using a fifth-order implicit backward differentiation formula algorithm, see, e.g., Ref. [3].

A total of 7 FE simulations has been carried out to assess the influence of the adopted energy pile layout and of the



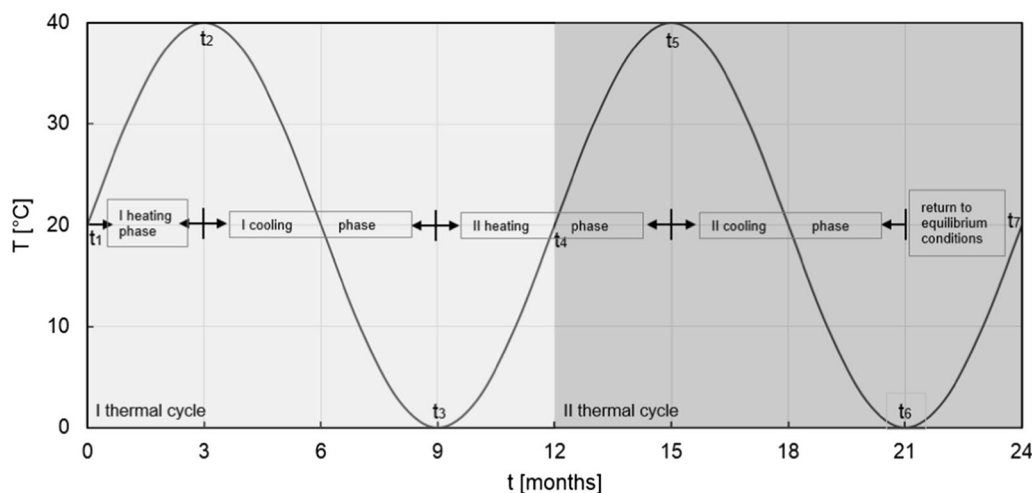
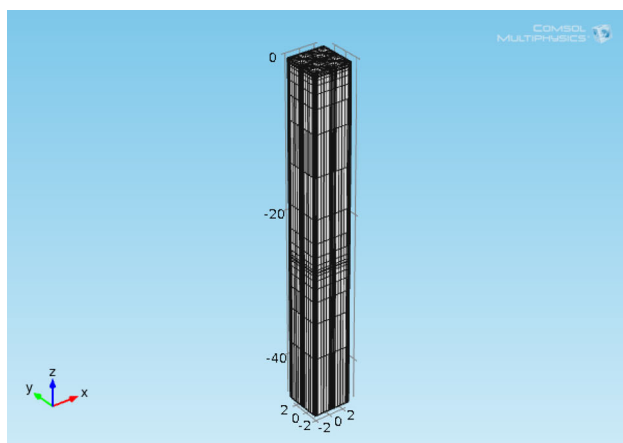
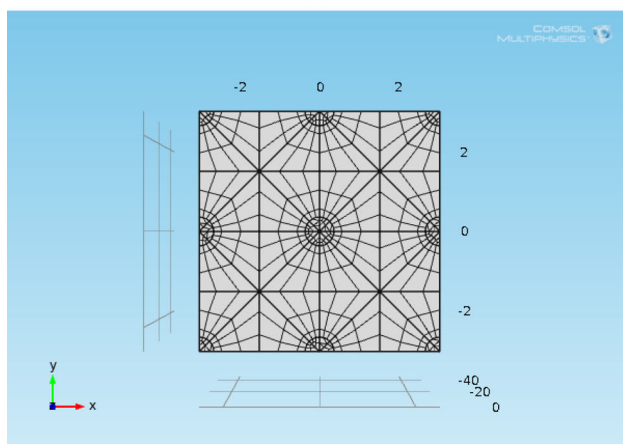


**Fig. 2** Thermal loading



**(a)**



**(b)**

**Fig. 3** Domain spatial discretization: **a** 3D view; **b** plane  $z = 0$

thermal properties of the soil. In particular, three different energy pile layouts have been considered for the unit cell under study (see Fig. 4). The first one (L1, hereafter referred to as the “reference case”) has only one thermo-

active pile at the center of the cell; in the second one (L2, with 3 full thermo-active piles) all the piles are thermo-active except the central one; finally, in the third one (L3, four full thermo-active piles) all the piles have been considered as thermo-active. In addition to the reference case, two additional values for the thermal expansion coefficient of the soil and for its thermal conductivity have been also considered. The complete program of the simulations is detailed in Table 2.

## 4 Results of the FE simulations

The main results of the group of simulations detailed in Table 2 are presented in this section. First, the response of the soil–foundation system to the operation of energy piles is discussed in detail for the reference case  $r01$ . Then, the effects of the variability of the soil thermal properties and of the energy pile layout are analyzed by comparing the reference case results with those from suitably selected simulations in the group.

### 4.1 Reference case

The thermo-hydro-mechanical effects induced in the soil–pile system by the operation of the energy piles in the reference case  $r01$ , with pile layout L1, are presented in the following, focusing on the spatial and temporal evolution of:

1. the axial load in each pile of the unit cell;
2. the vertical displacements of the raft.
3. the pore water pressure distribution in the soil.

Fig. 5 shows the evolution of the axial load  $N$  with depth for piles P9, P1 and P5, at the time stations reported in

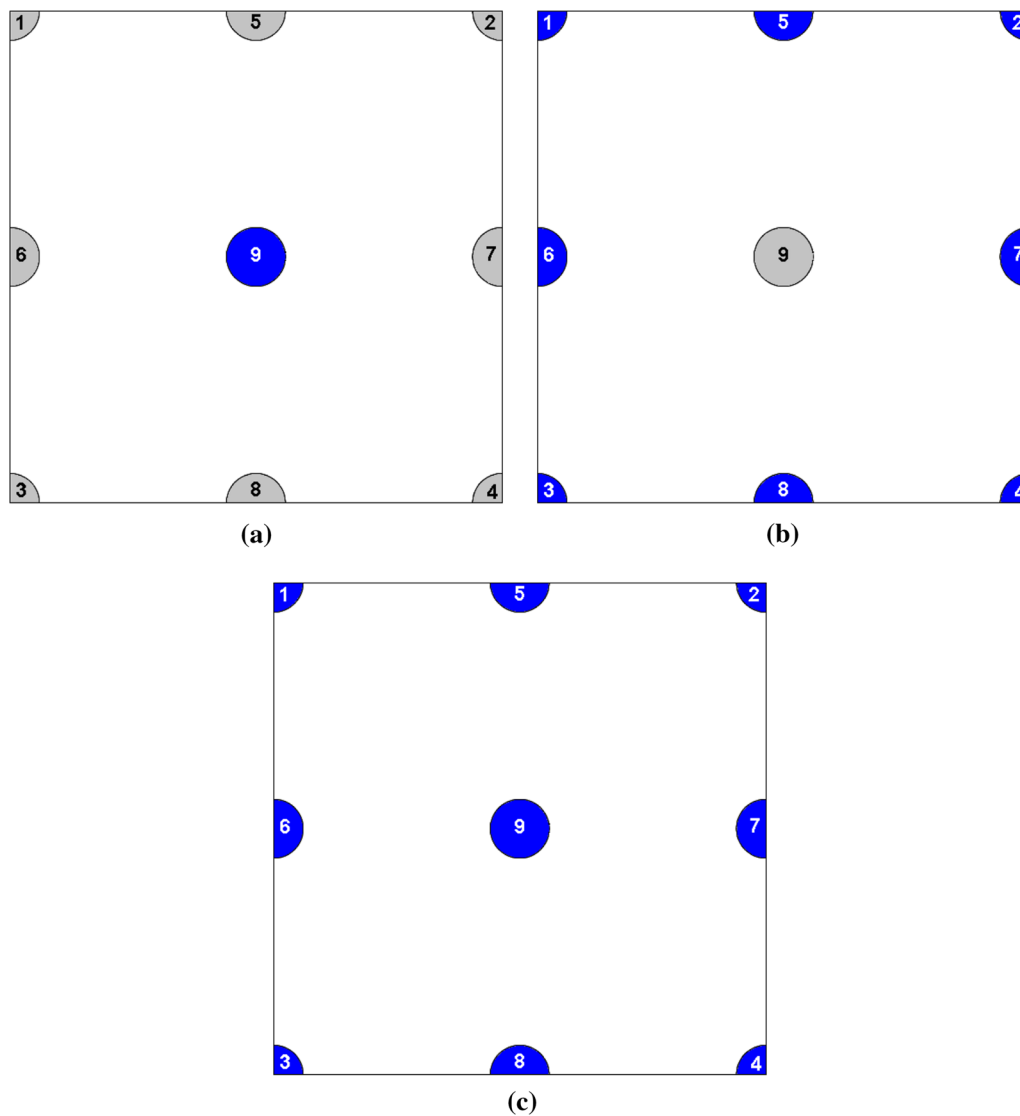


**Fig. 4** Energy pile layouts (thermo-active piles are shown in *dark blue*): **a** layout L1 with 1 thermo-active pile per cell; **b** layout L2 with 3 thermo-active piles per cell; **c** layout L3 with 4 thermo-active piles per cell (color figure online)

**Table 2** Program of the numerical simulations

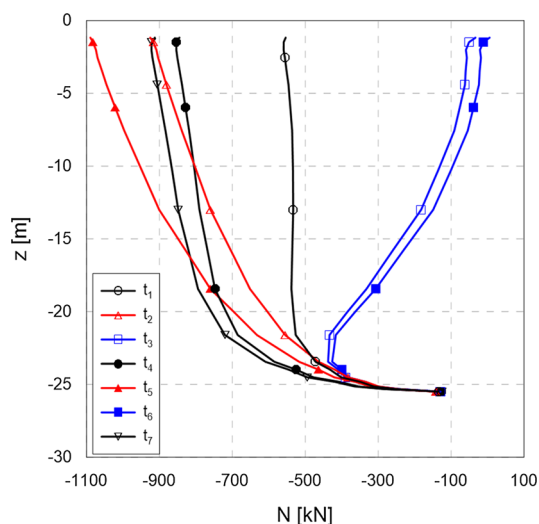
Analysis #	Energy pile layout	$\beta_s$ (1/K)	$\beta_{eff}$ (1/K)	$\lambda_{eff}$ [W/(mK)]
r01 (reference)	L1	$3.5 \times 10^{-5}$	$1.0 \times 10^{-4}$	1.7
r02	L1	$1.0 \times 10^{-5}$	$9.0 \times 10^{-5}$	1.7
r03	L1	$7.0 \times 10^{-5}$	$1.3 \times 10^{-4}$	1.7
r04	L1	$3.5 \times 10^{-5}$	$1.0 \times 10^{-4}$	0.9
r05	L1	$3.5 \times 10^{-5}$	$1.0 \times 10^{-4}$	2.5
r06	L2	$3.5 \times 10^{-5}$	$1.0 \times 10^{-4}$	1.7
r07	L3	$3.5 \times 10^{-5}$	$1.0 \times 10^{-4}$	1.7

Table 3. In the figure, negative values indicate compression, and positive values tension. Due to symmetry, the loads in corner piles P2, P3 and P4 are identical to those of

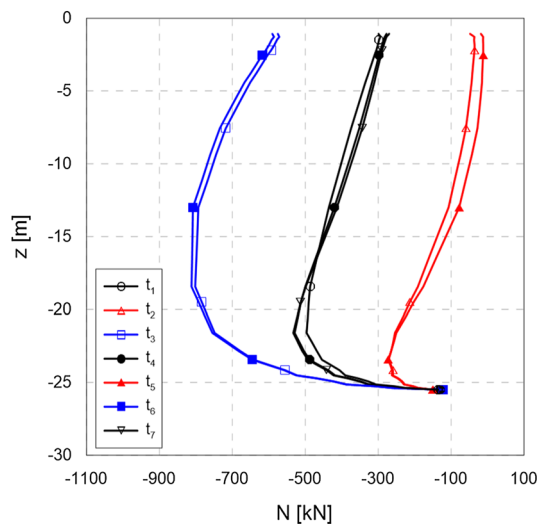
pile P1, and the loads in side piles P6, P7 and P8 are identical to those of pile P5.

The results show that the thermal dilation associated with the temperature increase in the time interval  $[t_1, t_2]$ , combined with the constraint provided by the stiff slab at the pile head movement, produces a significant increase in the compression load in pile P9 (Fig. 5a), up to a minimum value at the pile head of about  $-1100$  kN ( $\Delta N \simeq -550$  kN), in correspondence of the time station  $t_5$  (second heating stage).

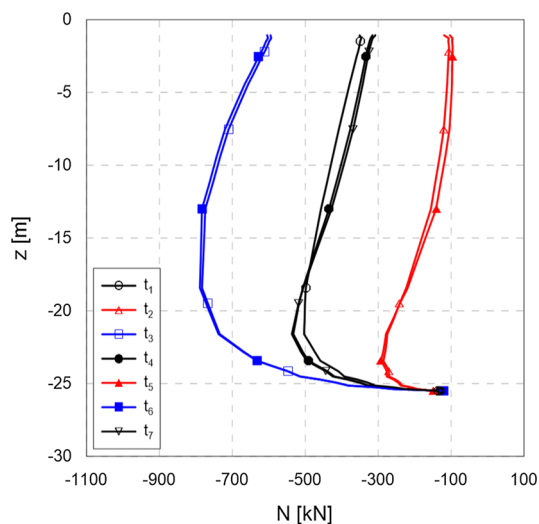
At the same time, the other piles of the group experience a substantial reduction in the compressive axial load, as a result of the upward incremental vertical displacement of the raft produced by the thermal dilation of the central thermo-active pile and of the surrounding region of soil



(a)



(b)



(c)

◀**Fig. 5** Isochrones of the axial load distributions  $N(z)$  along the piles at  $t = 0, 3, 9, 15, 21$  and  $24$  months: **a** pile P9 (thermo-active); **b** pile P1; **c** pile P5

**Table 3** Significant time stations

Time station	$t$ (months)	$T$ (°C)	Note
$t_1$	0	20	Initial equilibrium state
$t_2$	3	40	Maximum temperature, first cycle
$t_3$	9	0	Minimum temperature, first cycle
$t_4$	12	20	End of first cycle
$t_5$	15	40	Maximum temperature, second cycle
$t_6$	21	0	Minimum temperature, second cycle
$t_7$	24	20	End of second cycle

Column 3 provides the temperature of the thermo-active piles

where significant temperature changes have been experienced (see Fig. 5b, c).

During the first cooling phase, from  $t_2$  to  $t_3$ , the process is reversed: the thermo-active pile experiences a strong reduction in the axial compression load that, at the time of minimum temperature, is close to zero at the pile head ( $\Delta N \simeq +500$  kN). In the same period, the other piles of the group experience an increase in the axial compression load, as a result of the downward incremental vertical displacement of the raft associated with the thermal contraction of the central pile and of the surrounding soil region where a significant reduction in temperature has been experienced. In this case, the maximum  $\Delta N$  observed in P1 and P5 pile is smaller than that of P9 ( $\simeq -400$  kN, at a depth of about 13 m from the ground surface). The same pattern of behavior can be observed during the second heating-cooling cycle from  $t_4$  to  $t_7$ .

A complementary picture revealing the mechanical effects produced in the piles during the operation of the HVAC system is provided by Fig. 6, which shows the time evolution of the axial load in the thermo-active pile P9, at depths of  $z = -6$  m (section A),  $-13$  m (section B) and  $-20$  m (section C). Due to the complex interaction between the soil, the piles and the raft, the time stations at which the maxima and minima of  $\Delta N$  are observed do not coincide with the maxima and minima of the imposed temperature on the thermo-active pile surface, but correspond to slightly lower simulation times.

As far as axial loads on the piles are concerned, it is important to note that, in the presence of a thermal loading, the maximum compression load on the piles (experienced in this case at the thermo-active pile head) can reach values twice as high as those produced by mechanical loading, and significant additional deformations may be induced in



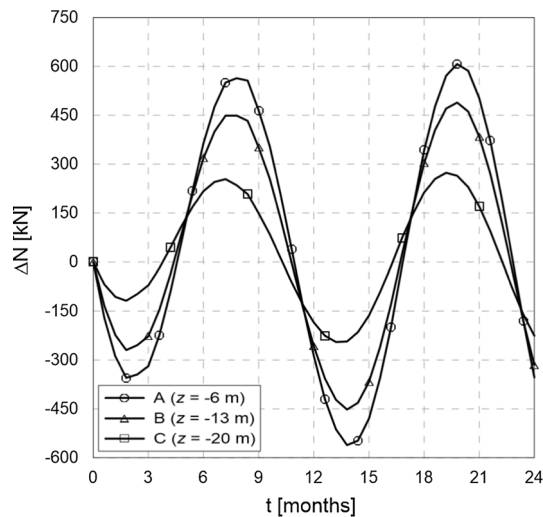


**Fig. 6** Evolution with time of the axial load variation,  $\Delta N$ , in pile P9 (thermo-active) at  $z = -6$   $-13$  and  $-20$  m

the structural elements. For this reason, assessing quantitatively the safety level with respect to both ultimate and serviceability limit states is of primary importance in energy pile design.

It is also important to note that the response of the thermo-active pile during the second thermal cycle does not coincide with the one observed during the first thermal cycle at shallow depths, because the displacement, temperature and pore pressure fields at the end of the first cycle do not show their respective initial conditions.

Figure 7 shows the contours of the thermally induced vertical displacements at the upper surface of the foundation raft,  $\Delta w(t) = w(t) - w(t_1)$ ; where  $w(t_1)$  is the vertical displacement at the end of the mechanical stage ( $-41$  mm). These are evaluated during the operation of the energy pile system at significant time stations of the first thermal cycle. In Fig. 7b, d, f, the contours of the temperature  $T$  at the same time stations are also shown.

The progressive heating of the soil region around the central thermo-active pile is responsible for a partial uplift of the raft, with a reduction of the vertical displacement  $\Delta w$  of about 10 mm (Fig. 7a) at  $t = t_2$ . This phenomenon, in turn, causes a net reduction of the loads in the outer, thermo-inactive piles of the group, as compared to the equilibrium conditions at the end of the initial mechanical loading stage. The opposite phenomenon occurs during the first cooling phase, from time station  $t_2$  to  $t_3$ , as the raft displacements start increasing up to values of about  $-50$  mm, that corresponds to a  $\Delta w$  of about  $-9$  mm (Fig. 7c). The same pattern of behavior is observed during the subsequent heating-cooling cycle. Note that—because of the high stiffness of the raft—the displacements are almost uniform at the raft surface, as they differ by only a few millimeters from point to point.

The above results refer to a linear isotropic elastic soil; however, the pattern of incremental displacements could be significantly different if plastic volumetric strains are induced by thermal softening effects as, for example, in soft clay soils, see e.g., [32].

Given the low permeability of the clay layer, the changes in soil temperature as well as the modifications in the total stress field induced by the operation of the energy pile give rise to changes in the pore pressure field that, in turn, affect the effective stress distribution and give rise to a transient water flow process within the soil mass. Figure 8a shows the distribution of the excess pore water pressure  $\Delta u = u(t) - u_0$  along a vertical profile placed at 0.6 m from the thermo-active pile axis. During the two heating stages ( $t_2$  and  $t_5$ ), positive excess pore pressures are predicted over the entire soil profile. On the other hand, negative excess pore pressures are obtained during the subsequent two cooling stages ( $t_3$ ,  $t_6$ ). Since the thermal expansion of pile P9 gives rise to a slight reduction in mean effective stress  $p'$  close to the pile during heating and to a corresponding increase in  $p'$  during cooling, this result can be explained only in terms of the differences existing between the water and the soil thermal expansion coefficients, with the former being much larger than the latter. The trend of  $\Delta u$  at the 3 points where the vertical crosses the horizontal sections A ( $z = -6$  m), B ( $z = -13$  m) and C ( $z = -20$  m), shown in Fig. 8b, confirms the previous observations. As expected, the smallest variations in pore water pressure occur at point A, closer to the upper draining boundary.

In general, the observed variations of pore water pressures are not large, ranging from a maximum value of about  $+20$  kPa to a minimum value of about  $-20$  kPa. In this respect, it is important to note that a quite different pattern of excess pore pressures could be obtained if the soil may undergo significant (contractant or dilatant) plastic strains, a possibility that in this case has not been considered.

Finally, Fig. 9 shows the effect of the temperature changes on the interaction between the soil, the piles and the connecting raft. In the figure, the red and black dashed curves provide the reference values, at the start of the energy pile operations, of the resultant vertical loads on the piles and at the contact between the soil and the raft, respectively. The full red and black curves give the same resultant loads, as a function of time, during the heating and cooling stages.

At the initial equilibrium condition, the total load transmitted to the piles is about 3 times the load directly transmitted by the raft to the soil at the soil-raft interface. During the subsequent operation of the energy piles, the resultant compressive load transmitted to the piles tends to

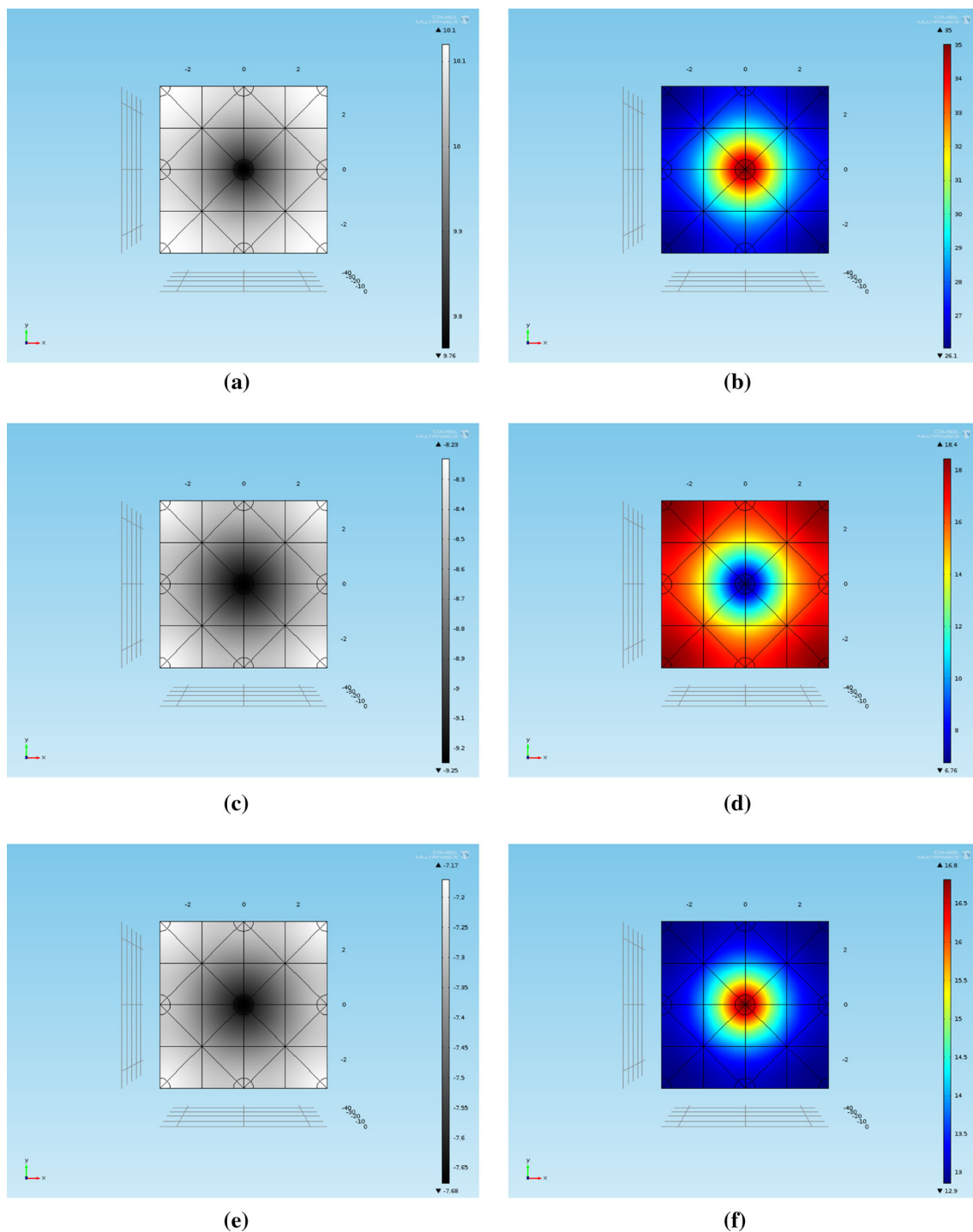


**Fig. 7** Contours of the thermo-induced vertical displacements of the raft,  $\Delta w(t)$ , (left column with values in mm) and contours of the temperature,  $T$ , (right column with values in °C) at different time stations: **a**, **b**  $t_2$ ; **c**, **d**  $t_3$ ; **e**, **f**  $t_4$

reduce during the heating stages and to increase during the cooling stages. Due to equilibrium, the resultant load transmitted by the raft to the soil shows an opposite trend. This result is consistent with the observations previously made on the evolution with time of pile loads and raft vertical displacements.

Again, the pattern of soil–pile–raft interaction shown in Fig. 9 could be substantially modified if temperature may cause the soil to yield, a possibility that in this case has not been considered.

The results in terms of structural loads, soil displacements and excess pore pressures, presented in the previous

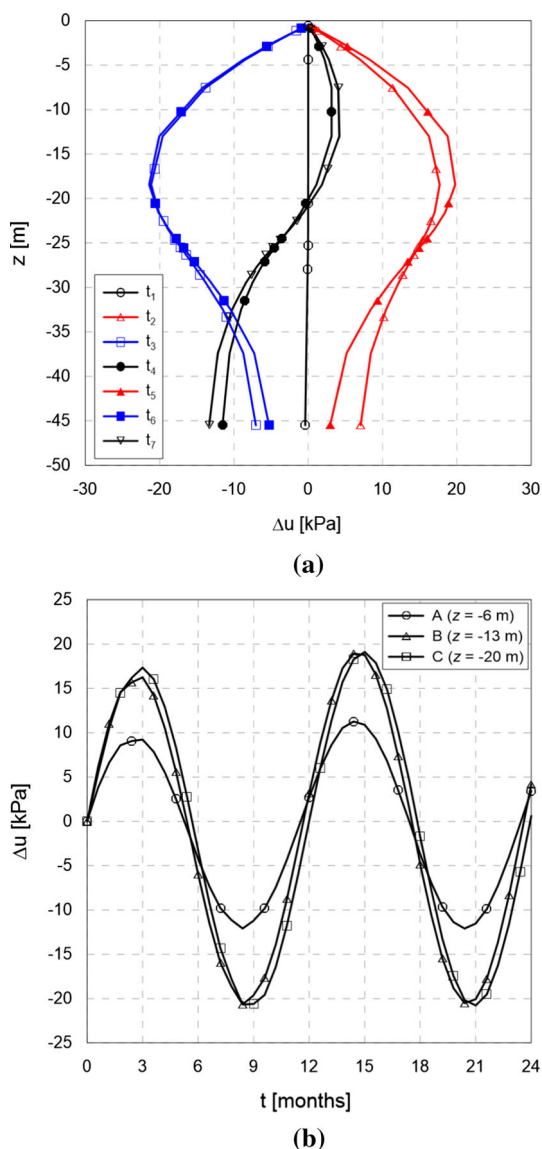


**Fig. 8** Excess pore water pressures in the vicinity of the thermo-active pile: **a** distributions of  $\Delta u$  along a vertical profile placed at 0.6 m from the pile axis at different time stations; **b** evolution of  $\Delta u$  with time at  $z = -6, -13$  and  $-20$  m along the same vertical profile

Figs. 5, 6, 7, 8 and 9 for the reference case, show that, regardless of the linearity of the soil response with respect to the assumed constitutive equations for the solid skeleton deformation and for the hydraulic and thermal flows, the system state at the end of each of the two thermal cycles is close, but not identical to the initial equilibrium conditions. This is due to the fact that the characteristic times associated with the two conduction processes (thermal and hydraulic) are either of the same order or larger than the period of the imposed temperature change at the thermo-active pile. This result might have important implications in long-term operations of large scale geothermal HVAC systems, the quantitative assessment of which would

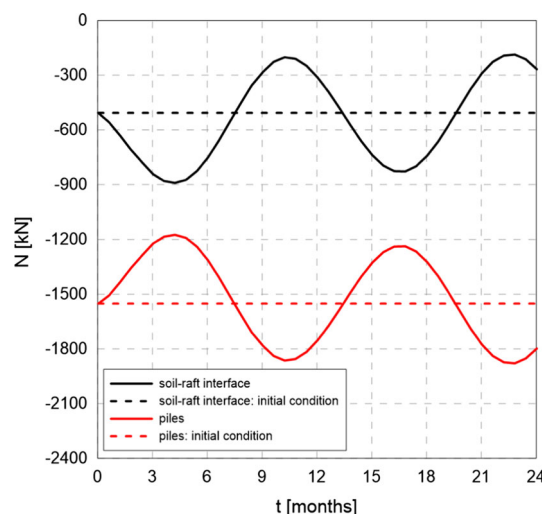


**Fig. 9** Redistribution of the resultant vertical load between the piles and the soil–raft interface upon thermal loading (color figure online)

require further numerical studies and long-term experimental observations in situ.

#### 4.2 Influence of the soil thermal expansion coefficient $\beta_{\text{eff}}$

The influence of the soil thermal expansion coefficient,  $\beta_{\text{eff}}$ , on the piled raft response to thermal loading conditions can be assessed by comparing the results of the reference case *r01* (performed with  $\beta_{\text{eff}} = 1.0 \times 10^{-4}$  1/K corresponding to a  $\beta_s = 3.5 \times 10^{-5}$  1/K) with those of two simulations performed with the same energy pile layout (L1) but with a smaller—*r02*—and a larger—*r03*—thermal expansion coefficient (see Table 2). To facilitate the interpretation of the results, only the first cycle of the thermal loading is considered in the following.

As expected, the thermal expansion coefficient of the solid skeleton affects the distribution of the axial load  $N$  along the pile shafts. This is clearly shown in Fig. 10, where the isochrones of  $N$  obtained in the three simulations are plotted at the time stations  $t_0$  to  $t_4$ , for the thermo-active pile P9 (Fig. 10a) and for pile P5 (Fig. 10b). While the three different solutions are qualitatively similar, they differ quantitatively in many respects. For P9, the compression loads at  $t = t_2$  (maximum heating) are lower than the reference solution for the higher  $\beta_{\text{eff}}$  and higher for the lower  $\beta_{\text{eff}}$ . The opposite is true at the time station  $t = t_3$  (maximum cooling). For P5, the heating stage corresponds to the minima of  $N$  and the cooling stage to the maxima of  $N$ , and the major variability is observed in the case of a higher value of  $\beta_{\text{eff}}$ . These results are in good agreement with the one obtained by [6, 34] and [8].

Figures 11 and 12 show the contours of the thermally induced vertical displacements,  $\Delta w$ , of the raft surface at

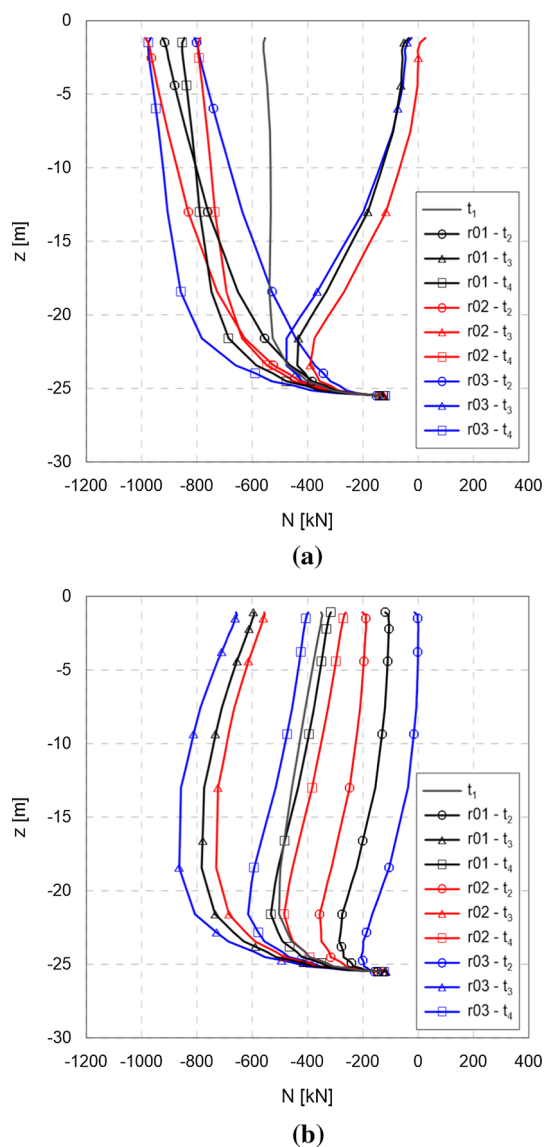


**Fig. 10** Effect of the thermal expansion coefficient  $\beta_{\text{eff}}$  on the axial load distribution in the piles at different time stations: **a** pile P9 (thermo-active); **b** pile P5

different time stations of the first thermal cycle for  $r02$  and  $r03$  simulations, respectively. In Figs. 11b, d, f and 12b, d, f, the contours of the temperature  $T$  at the same time stations are also shown.

To better understand the system behavior, the comparison between the time evolution of the vertical displacement,  $w$ , of the central pile head (pile P9) for  $r01$ ,  $r02$  and  $r03$  simulation is reported in Fig. 13. As can be noticed, the displacement due to the mechanical loading (equal to  $-41$  mm) is partially recovered during the heating phase, where the raft tends to move in the upward direction of about 8 mm for  $r02$  and 12 mm for  $r03$ . In the next cooling phase,  $w$  increases up to values greater than  $-50$  mm in all the cases. The worst-case scenario in terms of variability of

$w$  is represented by  $r03$  simulation, which is the one with the higher value of the soil thermal expansion coefficient.

Figure 14 shows the distribution of the excess pore water pressure  $\Delta u$  along a vertical profile placed at 1.2 m from the axis of the thermo-active pile, for the time stations  $t_2$ – $t_4$ . In this case, the quantitative differences between the three solutions appear limited, with the higher oscillations observed in the case of a higher  $\beta_{\text{eff}}$ .

### 4.3 Influence of the soil thermal conductivity $\lambda_{\text{eff}}$

The influence of the soil thermal conductivity,  $\lambda_{\text{eff}}$ , on the piled raft response to thermal loading conditions can be assessed by comparing the results of the reference case  $r01$  [performed with  $\lambda_{\text{eff}} = 1.7$  W/(mK)] with those of two simulations performed with the same energy pile layouts (L1) but with a smaller— $r04$ —and a larger— $r05$ —thermal conductivity (see Table 2). Again, to facilitate the interpretation of the results, only the first cycle of thermal loading is considered in the following.

An immediate effect of the increase (resp., decrease) of the soil thermal conductivity is the increase (resp., decrease) of the specific heat flux,  $H$ , from or to the thermo-active pile during heating/cooling. This is clearly shown by Fig. 15, which plots the evolution with time of  $H$  across the thermo-active pile surface, given by:

$$H = \frac{1}{A} \int_S \mathbf{q} \cdot \mathbf{n} \, da \quad (7)$$

where  $S$  is the external surface of the pile, and  $A$  is its total area. From the figure, it can also be observed that the period of oscillation of  $H$  changes slightly with thermal conductivity, increasing as  $\lambda_{\text{eff}}$  decreases.

Figures 16, 17 and 18 show the contours of the temperature,  $T$ , along the vertical plane  $x = 0$  for simulations  $r01$ ,  $r04$  and  $r05$ , respectively. In particular, Figs. 16a, 17a and 18a refer to time station  $t_2$  when the temperature is maximum during the first cycle; Figs. 16b, 17b and 18b refer to time station  $t_3$  when the temperature is minimum during the first cycle and Figs. 16c, 17c and 18c refer to time station  $t_4$  at the end of the first cycle. It can be observed that, although the temperature differences observed in the three cases are limited to a few degrees Celsius, the temperature around the thermally active central pile is more uniform in simulation  $r05$ , in which the thermal conductivity of the soil is the highest.

Figure 19 shows a detailed picture of the temperature distributions, plotted at some relevant time stations, along a vertical profile placed at 1.2 m from the thermo-active pile axis. The plot confirms that the larger the soil conductivity, the higher the temperature increase (or decrease) at a given distance from P9 pile axis.

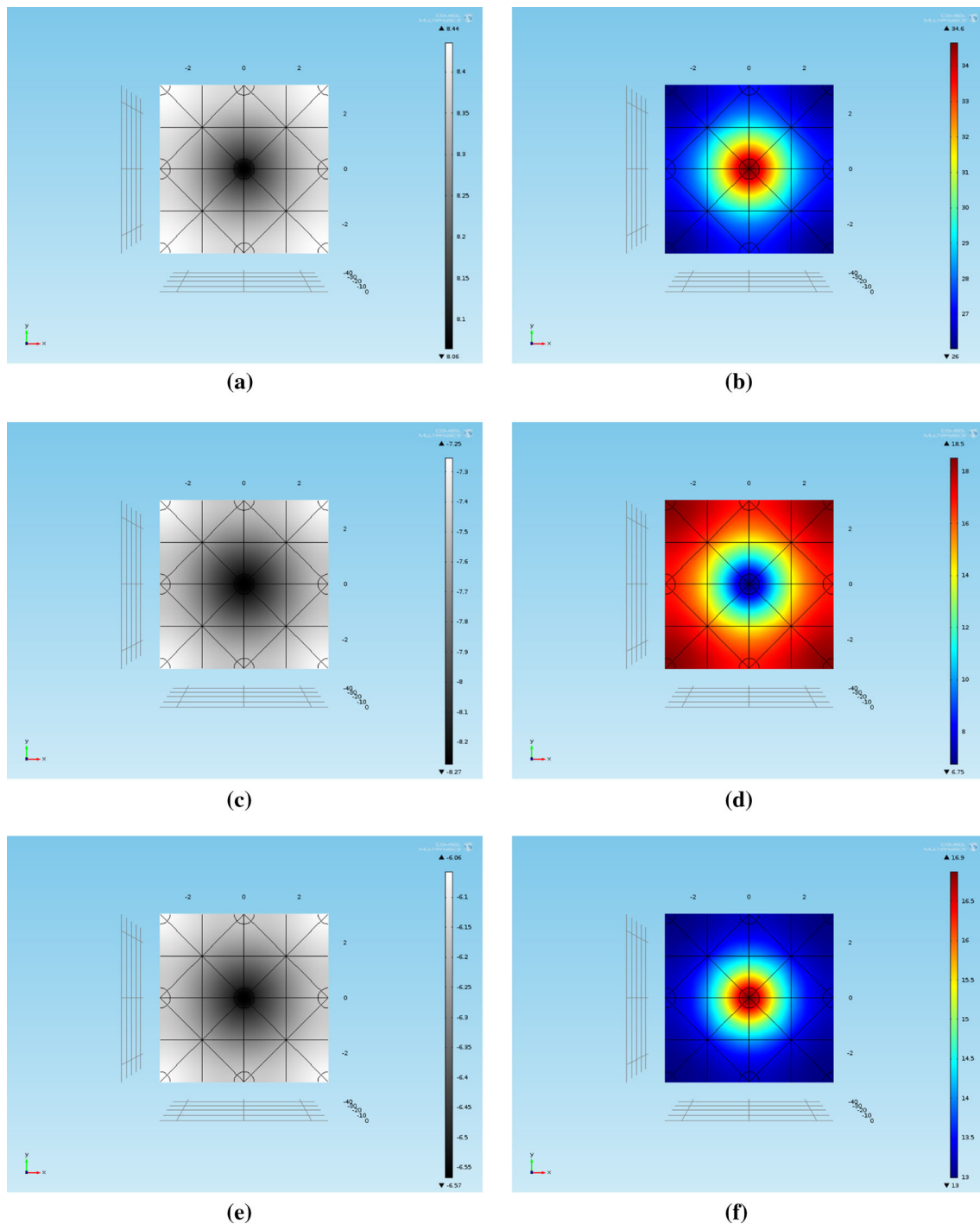


**Fig. 11** Contours of the thermo-induced vertical displacements of the raft,  $\Delta w(t)$ , (left column with values in mm) and contours of the temperature,  $T$ , (right column with values in °C) for  $r02$  simulation, at different time stations: **a, b**  $t_2$ ; **c, d**  $t_3$ ; **e, f**  $t_4$

The influence of the soil thermal conductivity on the axial load distribution of the piles is shown in Fig. 20. As compared to the reference solution, larger compressive loads during heating and smaller compressive loads during cooling are observed in the thermo-active pile for the case of lower thermal conductivity, while the opposite is true for the case of higher conductivity (Fig. 20a). From a

quantitative point of view, the differences observed among the three cases can be significant, with  $\Delta N$  values of  $\pm 100$  kN at the pile head. On the contrary, in pile P5, only minor differences in the axial load are obtained in the three simulations (Fig. 20b).

Figures 21 and 22 show the contours of the thermally induced vertical displacement,  $\Delta w$ , of the raft surface at



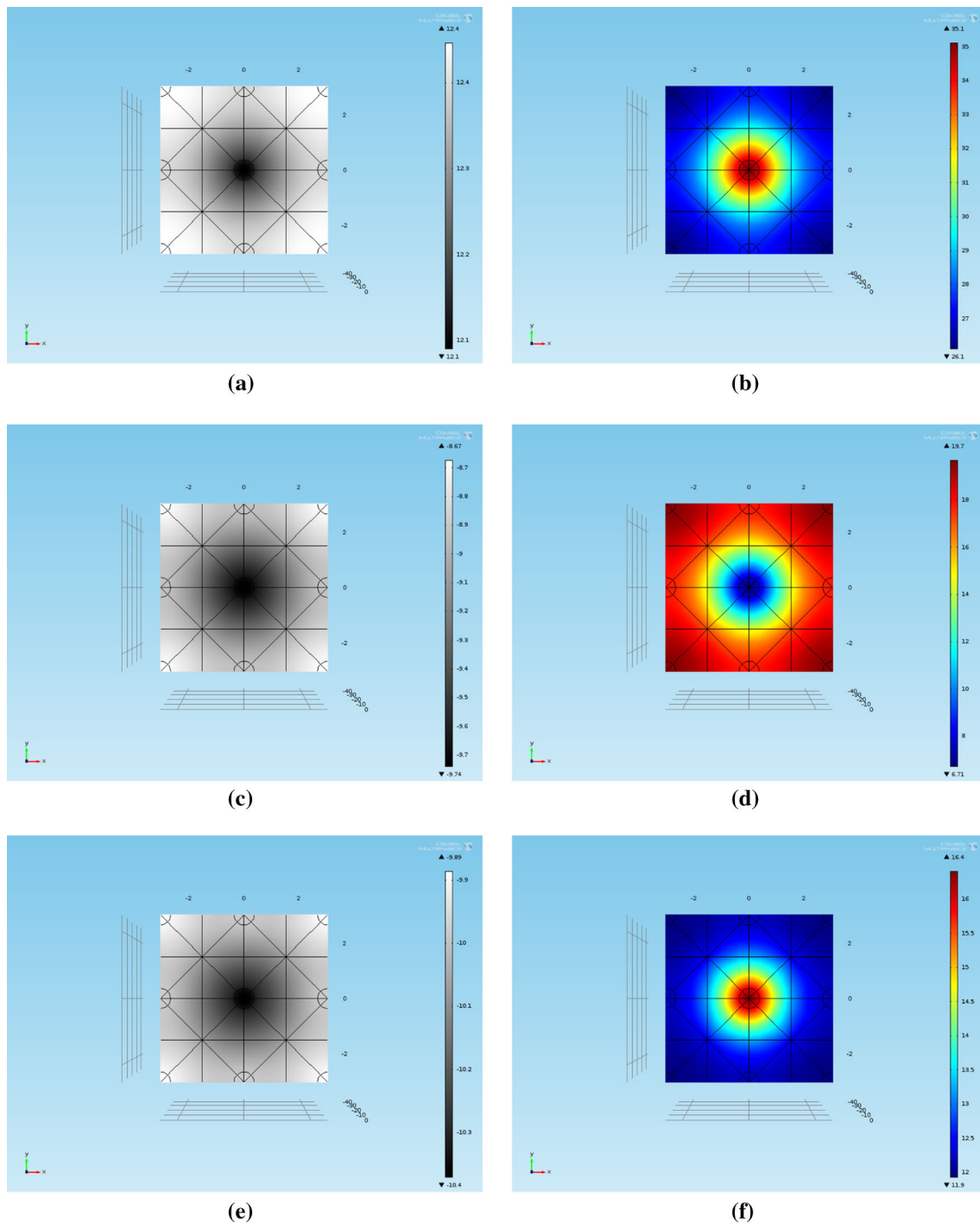


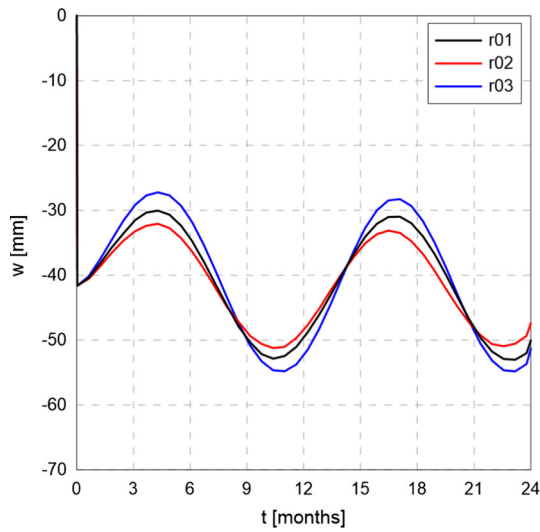
**Fig. 12** Contours of the thermo-induced vertical displacements of the raft,  $\Delta w(t)$ , (left column with values in mm) and contours of the temperature,  $T$ , (right column with values in °C) for  $r03$  simulation, at different time stations: **a, b**  $t_2$ ; **c, d**  $t_3$ ; **e, f**  $t_4$

different time stations of the first thermal cycle for  $r04$  and  $r05$  simulation, respectively. In Figs. 21b, d, f and 22b, d, f the contours of the temperature  $T$  at the same time stations are also shown.

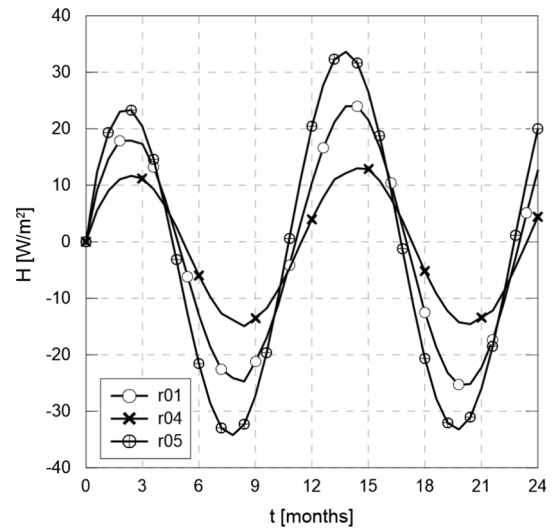
To better understand the system behavior, the comparison between the time evolution of the vertical displacement,  $w$ , of the central pile head (pile P9) for  $r01$ ,

$r04$  and  $r05$  simulation is reported in Fig. 23. As can be noticed, the displacement due to the mechanical loading (equal to  $-41$  mm) is partially recovered during the heating phase, where the raft tends to move in the upward direction of about 6 mm for  $r04$  and 12 mm for  $r05$ . In the next cooling phase,  $w$  increases up to values ranging between  $-48$  and  $-55$  mm. In this case the worst-case

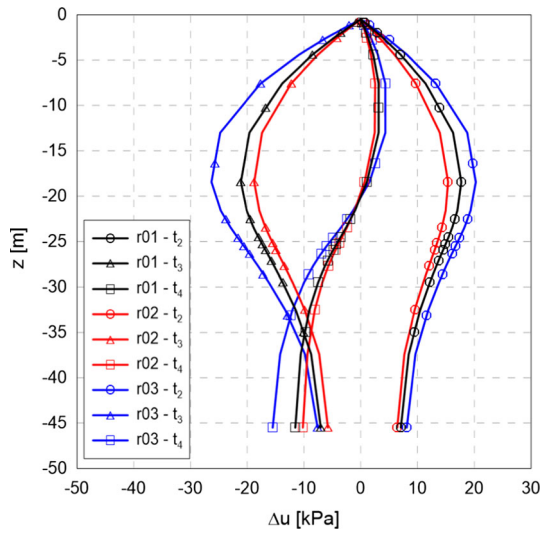




**Fig. 13** Comparison between  $r01$ ,  $r02$  and  $r03$  simulations: time evolution of the vertical displacement,  $w$ , of the central pile head (pile P9)



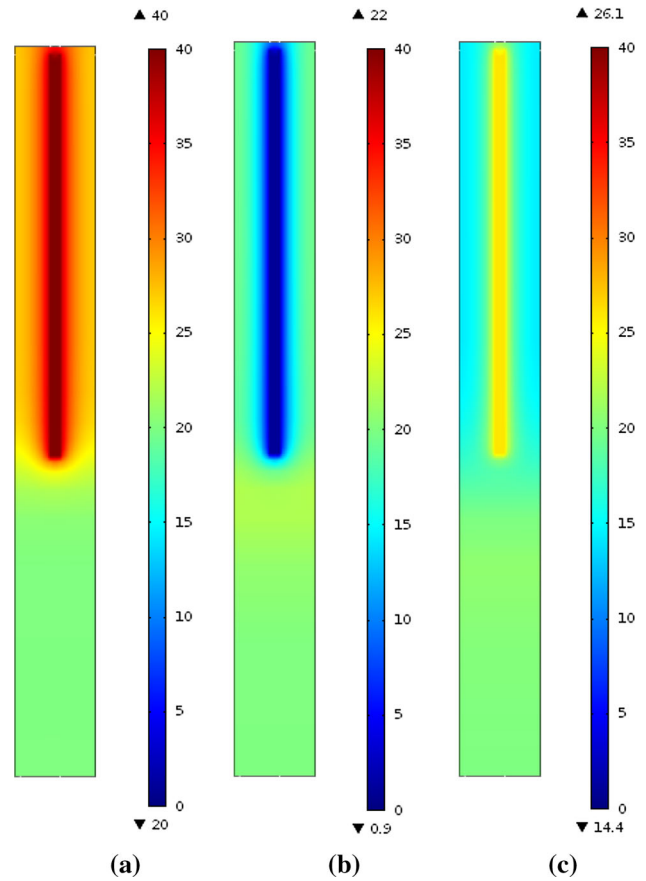
**Fig. 15** Time evolution of the specific heat flux,  $H$ , across the thermo-active pile lateral surface



**Fig. 14** Distributions of the excess pore water pressure,  $\Delta u$ , along a vertical placed at 1.2 m from the thermo-active pile axis at different time stations

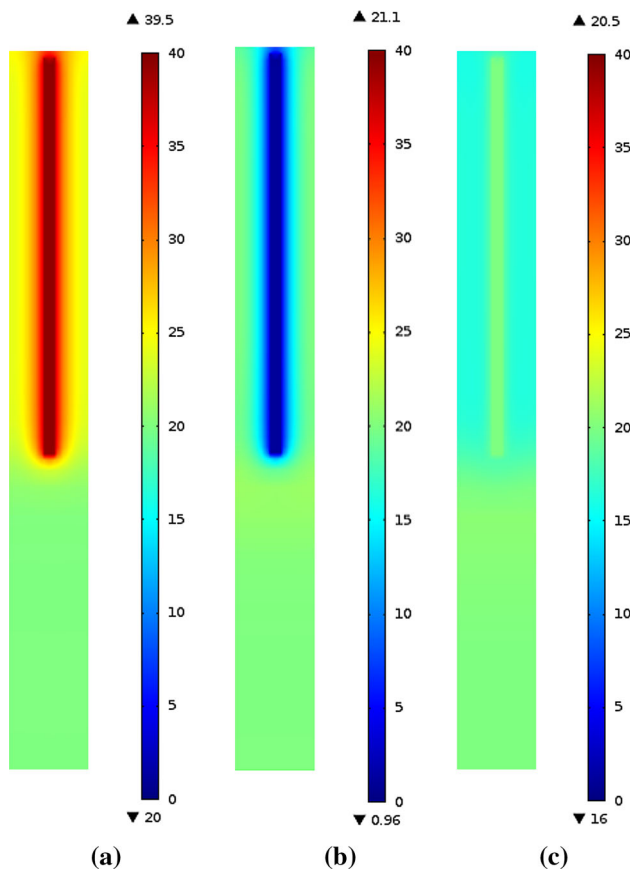
scenario in terms of  $\Delta w$  is represented by the  $r05$  simulation, which is the one with the greater value of the soil thermal conductivity.

Figure 24 shows the distribution of the excess pore water pressure along a vertical profile placed at 1.2 m from the thermo-active pile axis, at time stations  $t_2$ ,  $t_3$  and  $t_4$ , for the three simulations considered. The trends are consistent with those observed for the temperature changes along the same vertical profile: a larger conductivity yields to a larger temperature increments (resp., decrements) for the same elapsed time, and this, in turn, is associated to larger



**Fig. 16** Contours of the temperature,  $T$ , along the vertical plane  $x = 0$ , for  $r01$  simulation, at different time stations: **a**  $t_2$ ; **b**  $t_3$ ; **c**  $t_4$

negative (resp., positive)  $\Delta u$  values. Again, as in previous Sect. 4.2, the quantitative differences between the three solutions appear quite small in absolute terms.



**Fig. 17** Contours of the temperature,  $T$ , along the vertical plane  $x = 0$ , for  $r04$  simulation, at different time stations: **a**  $t_2$ ; **b**  $t_3$ ; **c**  $t_4$

#### 4.4 Effect of the energy pile layout

The last group of numerical simulation has been aimed at assessing the influence of the adopted energy pile layout within the group, by comparing the reference case  $r01$  (layout L1, with one thermo-active pile per cell) with  $r06$  (layout L2, with 3 thermo-active piles per cell) and  $r07$  (layout L3, with 4 thermo-active piles per cell) simulations, see Fig. 4.

The temperature distribution obtained at different time stations from the three simulations along a vertical profile placed at 1.2 m from the central pile axis are shown in Fig. 25. As expected, the larger is the number of energy piles, the larger are the (positive or negative) temperature changes experienced at any given time along the piles. This also means that, in the case of more than one thermo-active pile per cell, the temperature within the soil is more uniform than in the case of a single pile per cell (i.e., with a larger thermo-active pile spacing).

The differences in the temperature distributions associated with the three energy pile layouts considered have an important effect on the structural loads in the various piles of the cell, as can be observed from Fig. 26. In the figure,

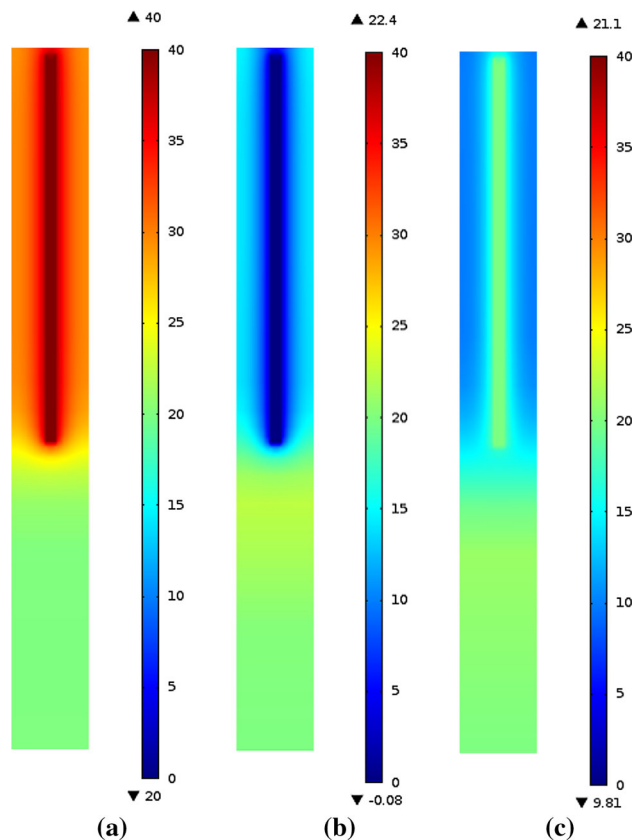


**Fig. 18** Contours of the temperature,  $T$ , along the vertical plane  $x = 0$ , for  $r05$  simulation, at different time stations: **a**  $t_2$ ; **b**  $t_3$ ; **c**  $t_4$

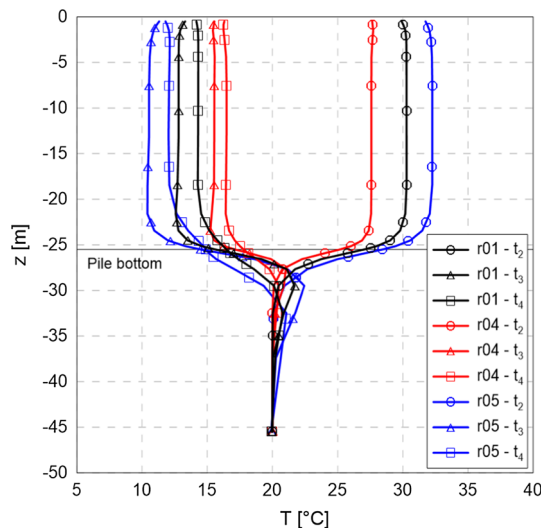


**Fig. 19** Distributions of the temperature,  $T$ , along a vertical profile placed at 1.2 m from the thermo-active pile axis at different time stations

the left column plots—Fig. 26a, c, e—compare the predicted distributions of the axial load  $N$  on piles P9, P1 and P5 at different time stations for layouts L1 and L2, while the right column plots— Fig. 26b, ,d, f—present the same comparison for layouts L1 and L3.

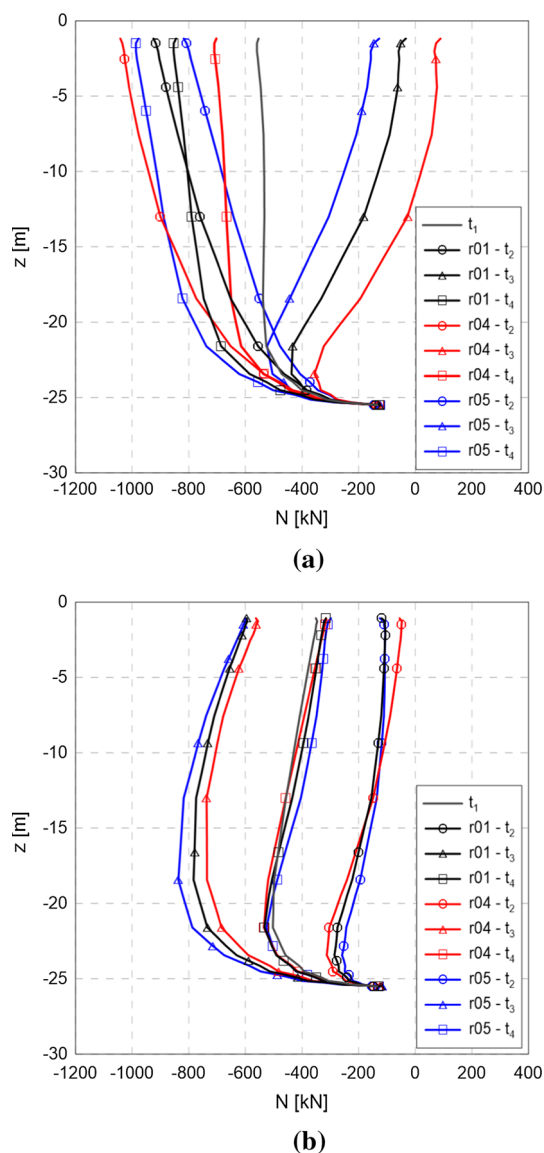


**Fig. 20** Effect of the thermal conductivity  $\lambda_{\text{eff}}$  on the axial load distribution in the piles at different time stations: **a** pile P9 (thermo-active); **b** pile P5

In the case of layout L3 (simulation  $r07$ ), the load distributions in piles P9 (central), P1 (corner) and P5 (side) are quite similar for all the time station considered. At  $t = t_2$  (heating) the axial loads are smaller than in the initial equilibrium conditions, while at  $t = t_3$  (cooling) axial load increase significantly, reaching a maximum compression load of about 900 kN at a depth of 20 m along the pile shaft. This phenomenon can be explained by considering that the thermal expansion coefficient of the clayey soil is 3.5 times larger than that of the concrete piles. As a consequence of the constraint exerted by the foundation raft to the vertical deformations of the soil, the contact pressures at the soil–raft interface increase with respect to the initial isothermal conditions during the heating stages, producing

a net decrease in the axial load at the pile heads. The opposite phenomenon occurs during the cooling stages, when the soil contracts more than the piles and the contact pressure at the soil–raft interface decreases.

The response of the soil–pile–raft system for layout L2 (simulation  $r06$ ) is similar to that observed for layout L3, with the only difference that the presence of a slightly smaller number of energy piles causes some quantitative differences between the loads computed in the central pile P9 as compared to the others. In particular, for this pile, the reductions in the axial load observed during heating and the increments observed during cooling are larger (in absolute terms) than for piles P1 and P5.

In comparison with the previous cases of layouts L2 and L3, it is noteworthy that the response observed at the central thermo-active pile P9 for layout L1 (reference case  $r01$ ) is completely different from a qualitative point of view, see Fig. 26a, b). In fact, when P9 is the only thermo-active pile, the axial compression loads increase during the heating stage ( $t = t_2$ ) and decrease during the cooling stage ( $t = t_3$ ). This phenomenon is due to the fact that the fraction of the soil that is affected by significant temperature changes during the thermal cycle remains relatively limited when only one thermo-active pile is present in the unit cell (i.e., when the thermo-active pile spacing is relatively large). The resultant of the axial loads at the pile heads still decreases during heating and increases during cooling as in the other cases considered (see Fig. 9). However, the thermal dilation of the central pile is sufficient in this case to produce an increment in the axial compression load on this single pile, while the response of the other piles remains similar to what has been observed for the thermo-active pile layouts L2 and L3 (see Fig. 26c–f).

Figures 27 and 28 show the contours of the thermally induced vertical displacements,  $\Delta w$ , of the raft surface at different time stations of the first thermal cycle for  $r10$  and  $r11$  simulation, respectively. In Figs. 27b, d, f and 28b, d, f, the contours of the temperature  $T$  at the same time stations are also shown.

To better understand the system behavior, the comparison between the time evolution of the vertical displacement,  $w$ , of the central pile head (pile P9) for  $r01$ ,  $r06$  and  $r07$  simulation is reported in Fig. 29. As can be noticed, the displacement due to the mechanical loading (equal to  $-41$  mm) is partially recovered during the heating phase, where the raft tends to move in the upward direction of about 20 mm for both  $r06$  and  $r07$ . In the next cooling phase,  $w$  increases up to values ranging between  $-52$  and  $-65$  mm. As can be expected, the variability of  $w$  increases with the increasing number of the energy piles in the foundation. The presence of several thermo-active elements can lead to variations in the raft depth of more than

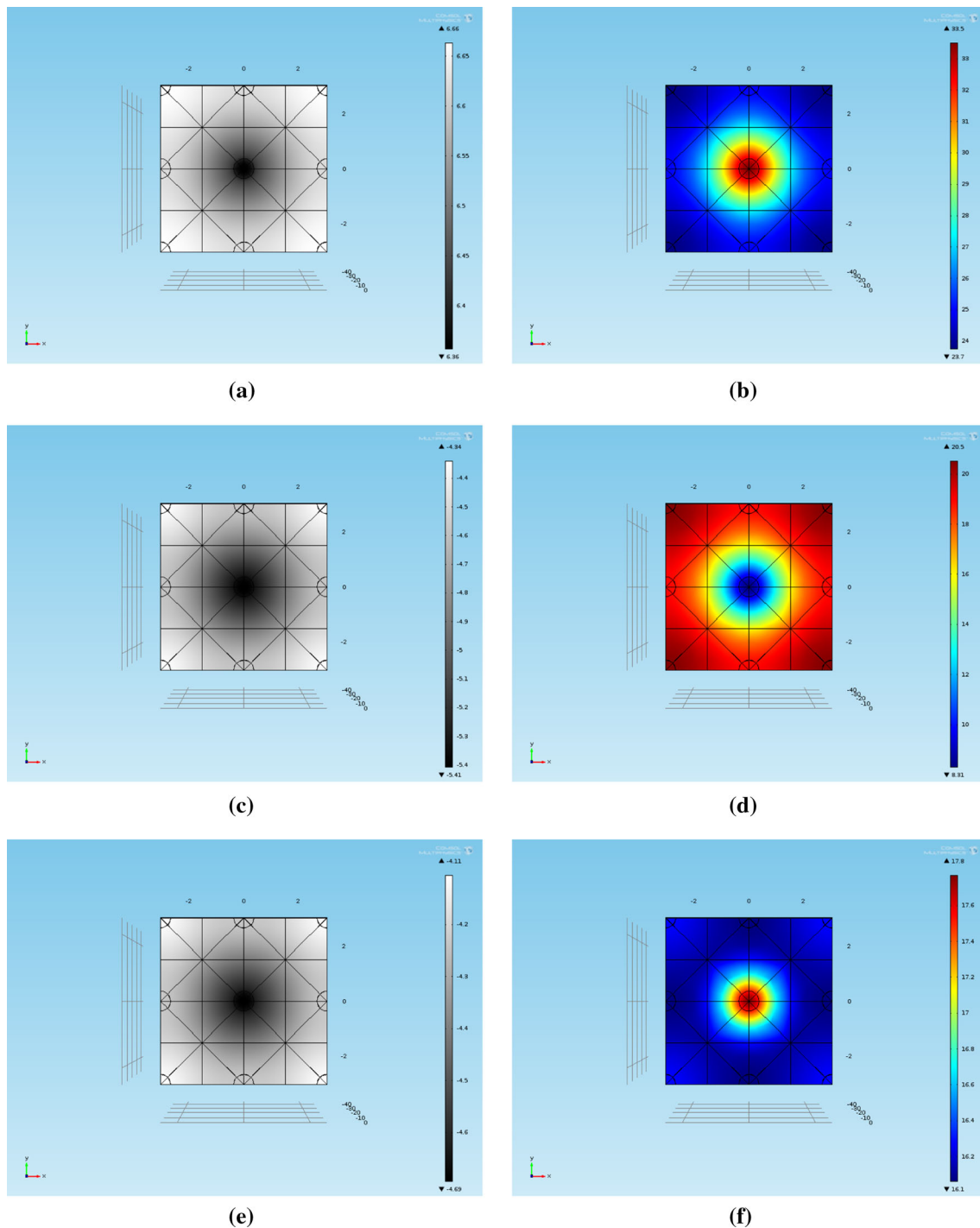


**Fig. 21** Contours of the thermo-induced vertical displacements of the raft,  $\Delta w(t)$ , (left column with values in mm) and contours of the temperature,  $T$ , (right column with values in °C) for  $r04$  simulation, at different time stations: **a, b**  $t_2$ ; **c, d**  $t_3$ ; **e, f**  $t_4$

2 cm with respect to those induced by the mechanical loading.

Figure 30 shows the distribution of excess pore water pressure along a vertical profile placed at 1.2 m from the thermo-active pile axis, for different time stations. Fig. 30a compares the results obtained for L1 and L2

layouts; Fig. 30b show the comparison for pile layouts L1 and L3. From a qualitative point of view, the effect of the increment of the number of thermo-active piles in the cell is similar to that observed in the case of a higher thermal conductivity for the soil (see Fig. 24, blue curves). In fact, all these scenarios correspond to more uniform and larger

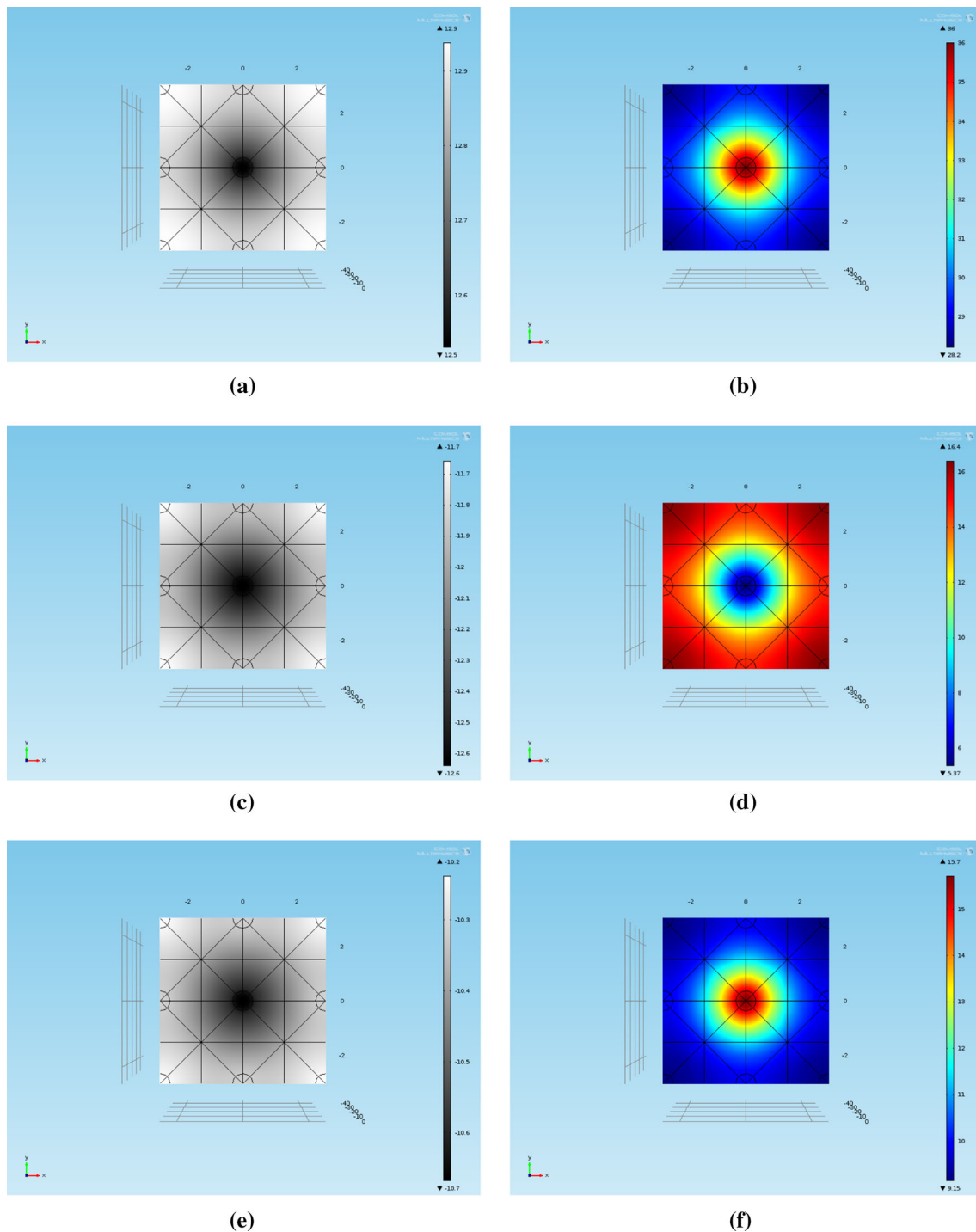


**Fig. 22** Contours of the thermo-induced vertical displacements of the raft,  $\Delta w(t)$ , (left column with values in mm) and contours of the temperature,  $T$ , (right column with values in  $^{\circ}\text{C}$ ) for r05 simulation, at different time stations: **a, b**  $t_2$ ; **c, d**  $t_3$ ; **e, f**  $t_4$

temperature variations in the soil. During the thermal cycle, a larger temperature increment (resp., decrement) for the same elapsed time, gives rise to larger negative (resp., positive)  $\Delta u$  values. Differently from the case discussed in Sect. 4.3, the quantitative differences between the reference solution and the others are not that

small in absolute terms, although the maximum and minimum values of  $\Delta u$  remain within the range  $[-40, +40]$  kPa. It is interesting to note that the excess pore pressure profiles for layouts L2 and L3 at the end of the cycle ( $t = t_4$ ) are quite off the initial condition at the start of the cycle ( $\Delta u = 0$ ). This allows to extend the

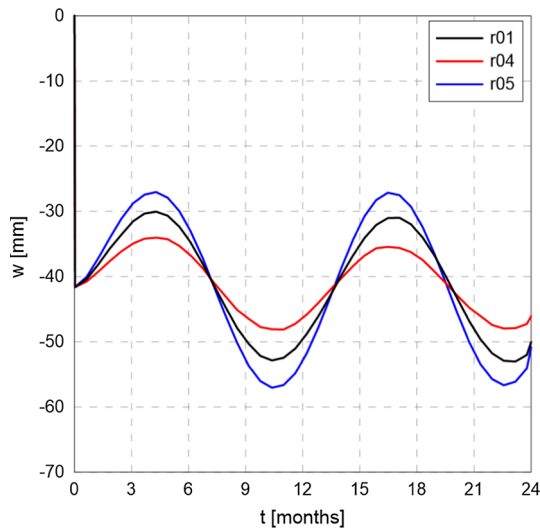


**Fig. 23** Comparison between *r01*, *r04* and *r05* simulations: time evolution of the vertical displacement, *w*, of the central pile head (pile P9)

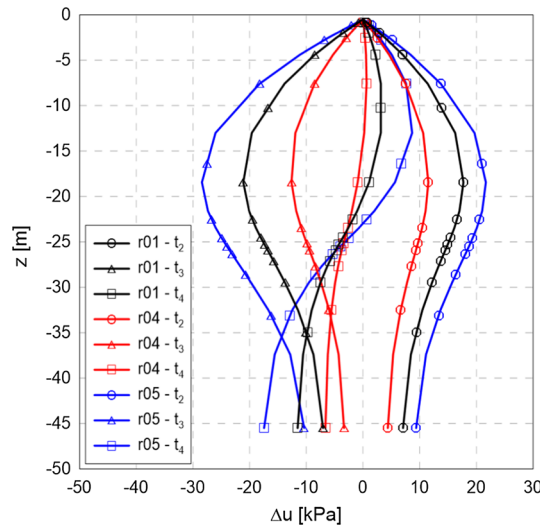
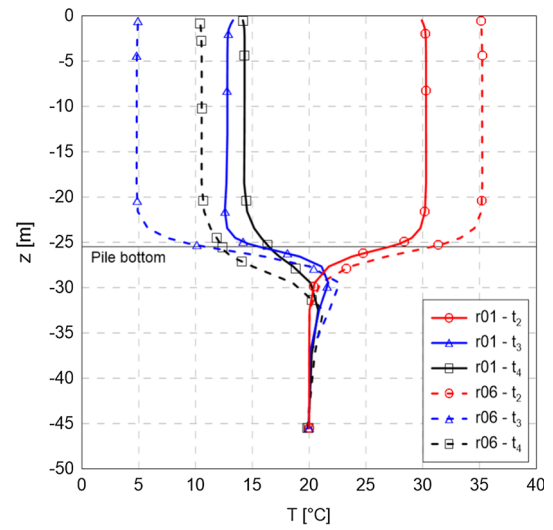


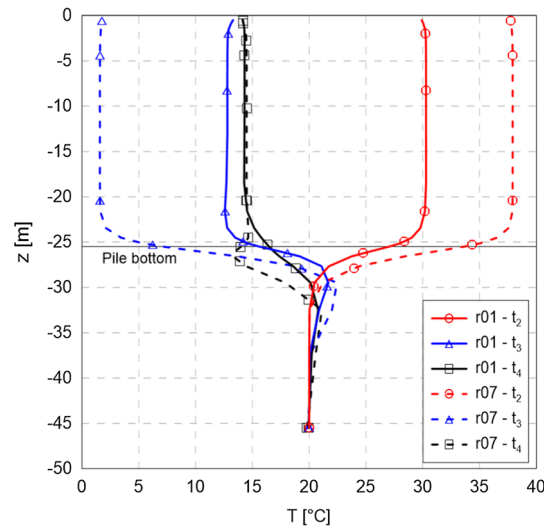
**Fig. 24** Distributions of the excess pore water pressure,  $\Delta u$ , along a vertical profile placed at 1.2 m from the thermo-active pile axis, at different time stations (color figure online)

observations made at the end of Sect. 4.1 to the other pile layouts considered.

An important aspect that may affect the overall performance of the HVAC system when closely spaced energy piles are used—such as in *r06* and *r07*—is the possible interference between the piles caused by the overlapping influence zones of each pile during the heating or cooling stages. This phenomenon can be assessed quantitatively by comparing the evolution with time of the specific heat flux, *H*, across the lateral surface of all the thermo-active piles, defined as:



(a)



(b)

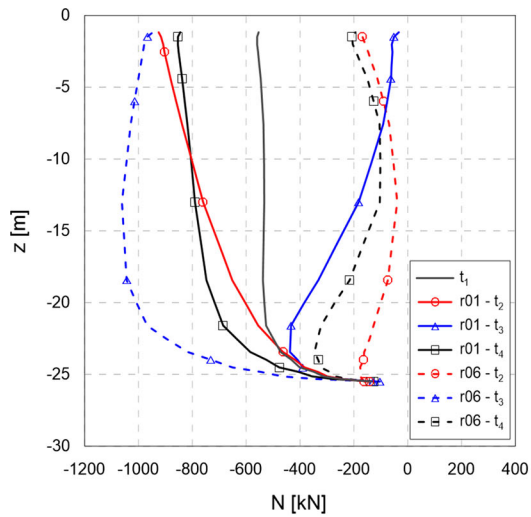
**Fig. 25** Distributions of the temperature, *T*, along a vertical profile placed at 1.2 m from P9 pile axis, at different time stations: **a** comparison between reference case *r01* and case *r06*; **b** comparison between reference case *r01* and case *r07*

**Fig. 26** Isochrones of the axial load distributions *N*(*z*) along piles P9, P1 and P5 at time stations *t*<sub>1</sub>–*t*<sub>4</sub>: comparison between reference case *r01* (pile layout L1) and cases *r06* (layout L2) and *r07* (layout L3)

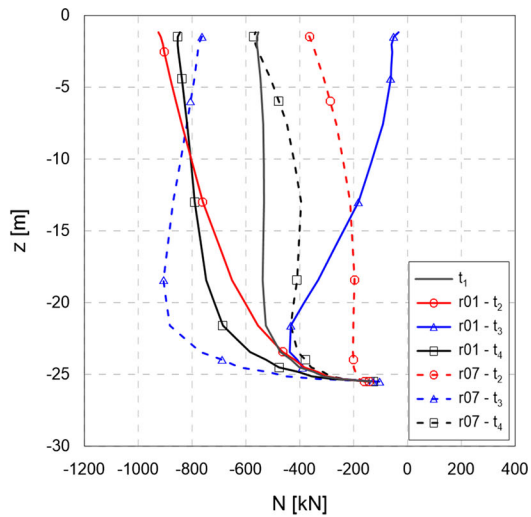
$$H = \frac{1}{\sum_{i=1}^{n_{ap}} A_i} \sum_{i=1}^{n_{ap}} \left( \int_{S_i} \mathbf{q} \cdot \mathbf{n} da \right) \tag{8}$$

where the sums are extended to all the *n*<sub>ap</sub> thermo-active piles of the cell; Eq. (8) reduces to Eq. (7) in the case of a single thermo-active pile.

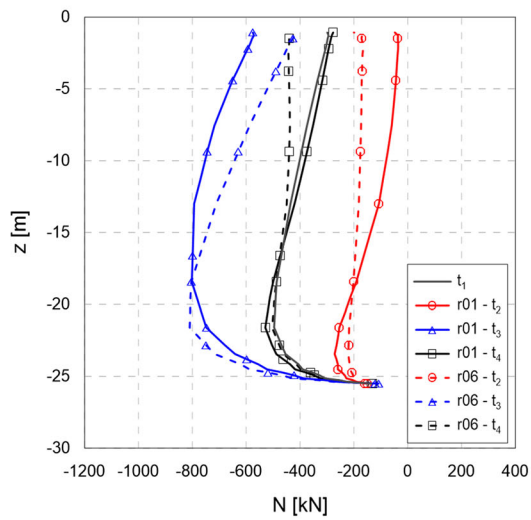




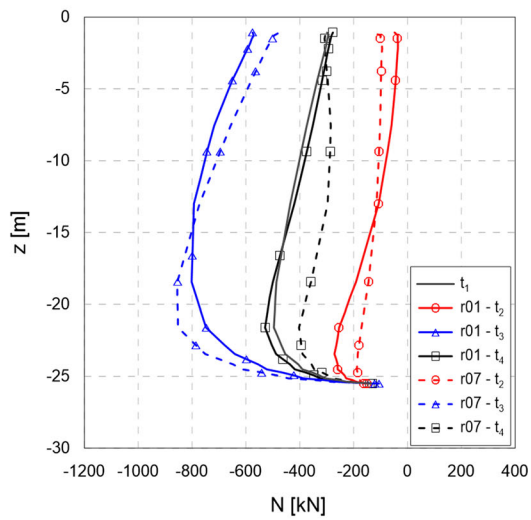
(a)



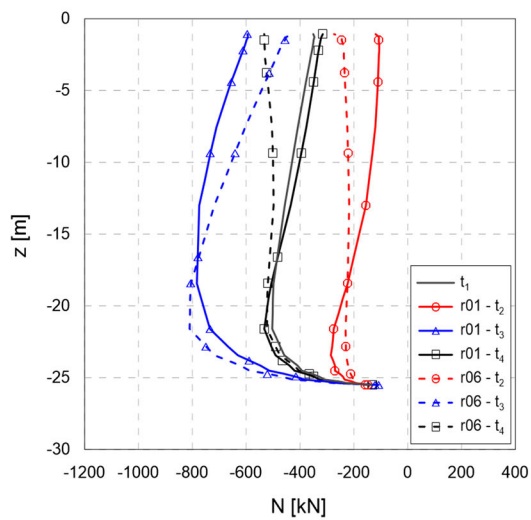
(b)



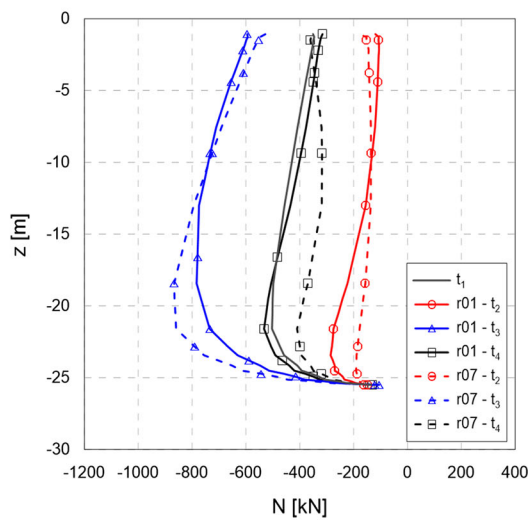
(c)



(d)



(e)



(f)

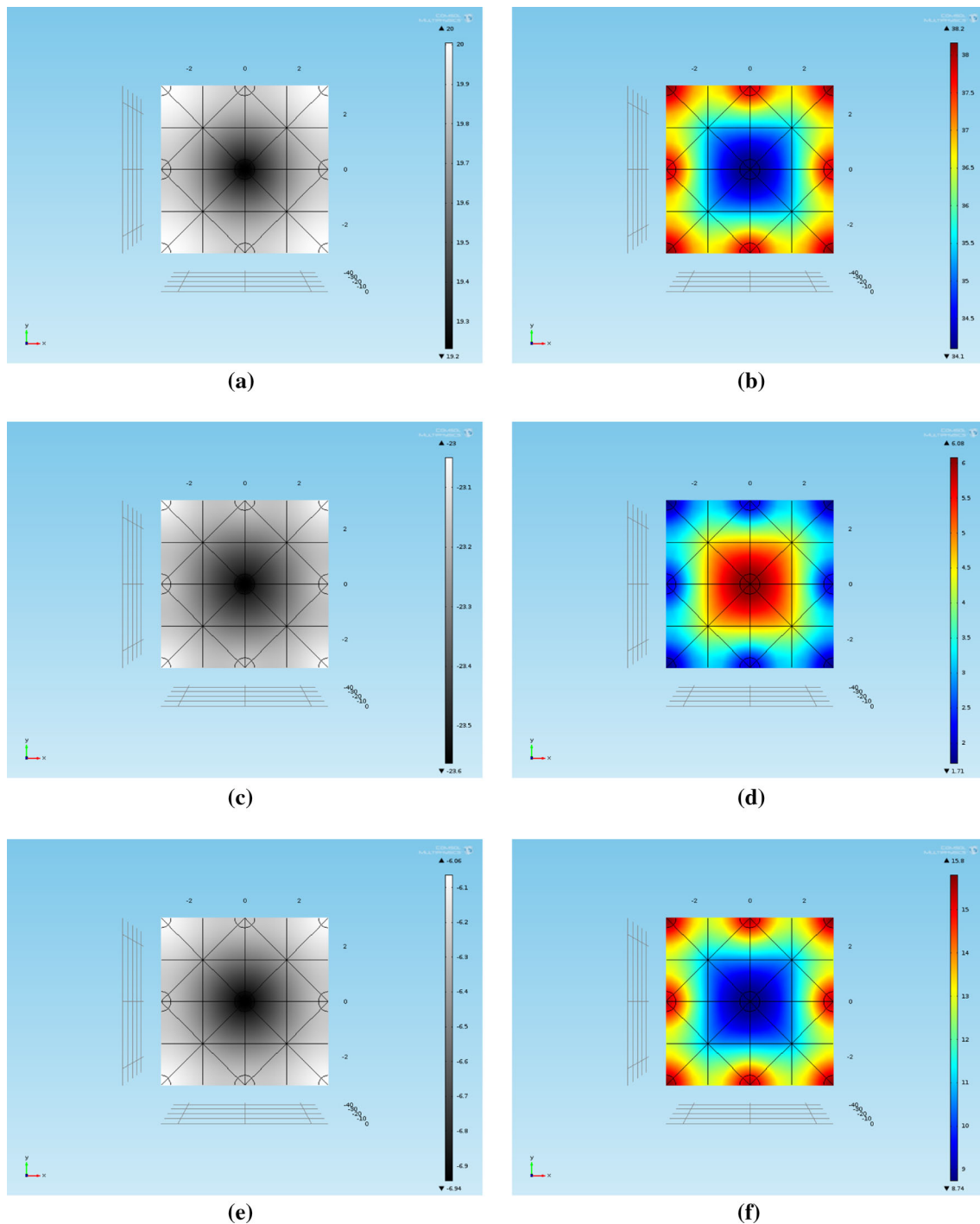


**Fig. 27** Contours of the thermo-induced vertical displacements of the raft,  $\Delta w(t)$ , (left column with values in mm) and contours of the temperature,  $T$ , (right column with values in °C) for  $r06$  simulation, at different time stations: **a, b**  $t_2$ ; **c, d**  $t_3$ ; **e, f**  $t_4$

Figure 31 shows the evolution with time of  $H$  for the three energy pile layouts considered. From the figure, it can be noted that the peaks of the specific heat flux in the case of the single central thermo-active pile is always larger (resp. smaller) than in the other two cases considered. This is due to the effect of thermal interference among the different thermo-active piles in the cell. This effect is rather

significant; in fact, the average total positive heat outflux during heating is about  $20 \text{ W/m}^2$  for layout L1,  $37.5 \text{ W/m}^2$  for layout L2 and  $44 \text{ W/m}^2$  for layout L3. This indicates that adding more piles to a finite dimension cell does not lead to a proportional increase in the system efficiency, since the value of  $H$  in layout L2 is about 1.88 times larger

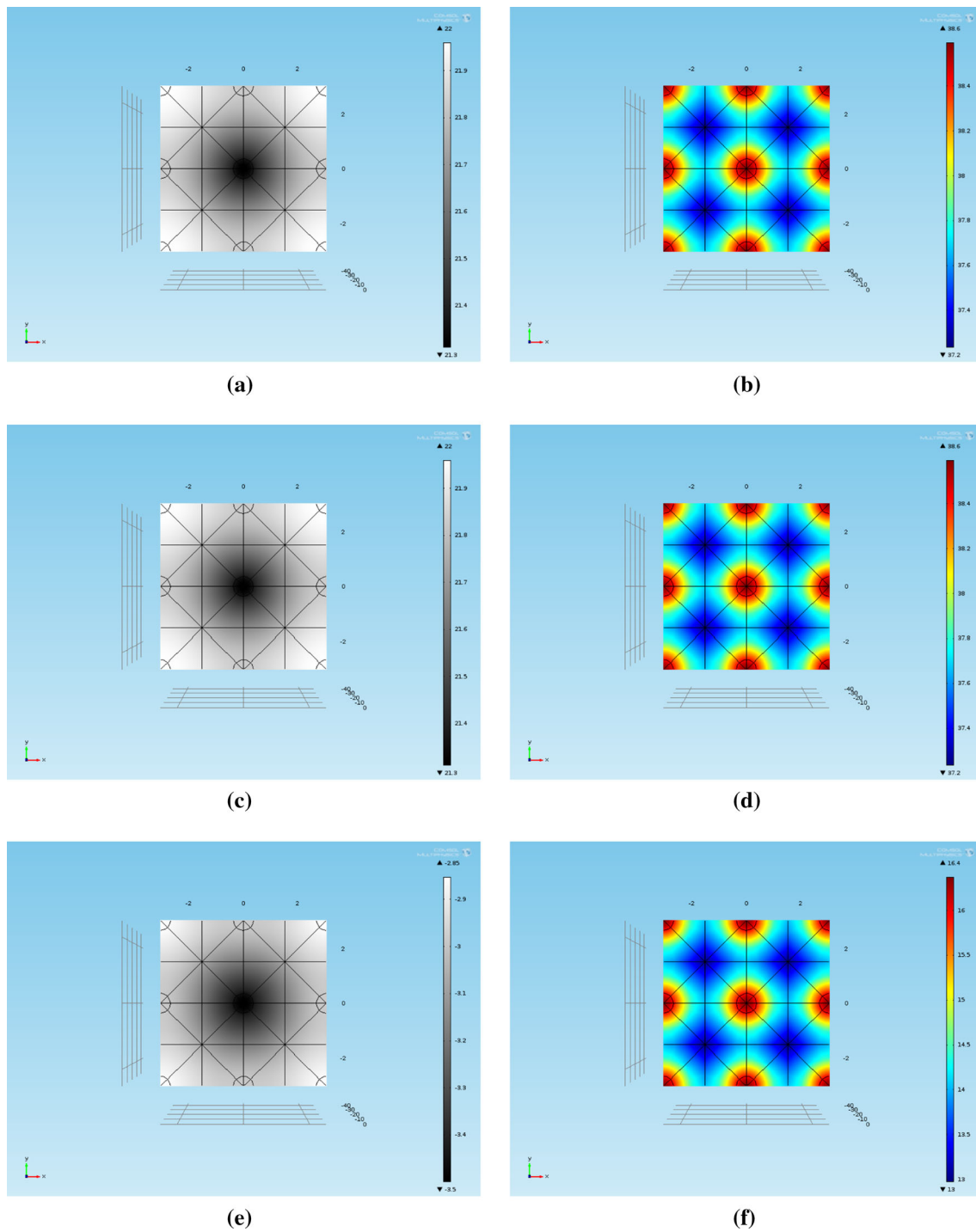


**Fig. 28** Contours of the thermo-induced vertical displacements of the raft,  $\Delta w(t)$ , (left column with values in mm) and contours of the temperature,  $T$ , (right column with values in  $^{\circ}\text{C}$ ) for r07 simulation, at different time stations: (a) and (b)  $t_2$ ; c, d  $t_3$ ; e, f  $t_4$

than the reference value (instead of 3), and in layout L3 is only about 2.2 times larger than the reference value (instead of 4). Similar considerations can be made with reference to the cooling stages. In this respect, layout L2 appears to be preferable to layout L3, for which the interference effects are significant.

## 5 Concluding remarks

A series of fully coupled 3D THM FE analyses has been conducted to investigate the effects of the thermal changes imposed by the regular performance of a GSHP system driven by energy piles on a very large piled raft.

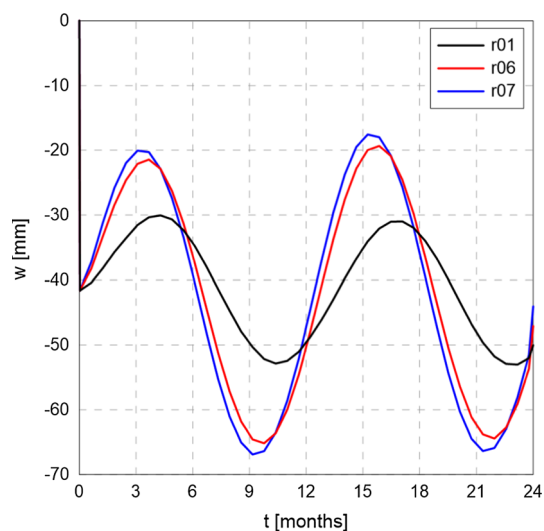
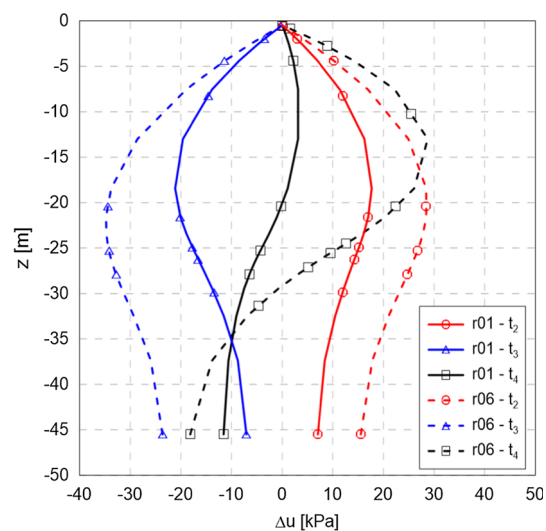


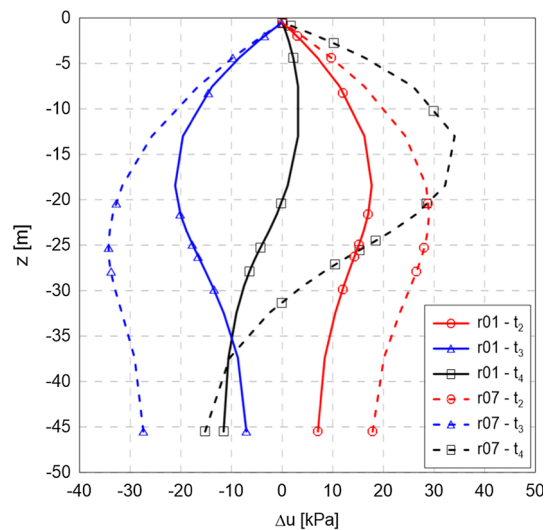
**Fig. 29** Comparison between  $r01$ ,  $r06$  and  $r07$  simulations: time evolution of the vertical displacement,  $w$ , of the central pile head (pile P9)

The results of the numerical simulations have shown that the soil–pile–raft interaction effects can be very important. In particular the following points are worth mentioning:

- the presence of a relatively rigid raft in direct contact with the soil is responsible for axial load variations in inactive piles of the same order of those experienced by the thermo-active piles, even when the latter are relatively far apart and temperature changes in inactive piles are small. In all the cases considered, the changes in the pile loads as well as the changes in the contact pressures at the soil–raft interface are significant and should not be neglected in the structural design of the foundation;
- while compression loads in inactive piles always increase during the cooling stages and decrease during the heating ones, the axial load changes in the thermo-active piles depend on pile spacing. For widely spaced thermo-active piles—as in the case of layout L1—compression loads increase during heating and decrease during cooling; the opposite occurs when the thermo-active piles are tightly spaced;
- when the soil is characterized by a low permeability, transient pore water pressure variations can be induced in the soil as a consequence of temperature changes. For all the cases considered, in which the stiff clay soil has been modeled as an isotropic elastic material, pore water pressure changes are associated with differential thermal dilations between the solid skeleton and the pore water, as well as to total stress changes under partially drained conditions, and remain relatively small;



**(a)**



**(b)**

**Fig. 30** Distributions of the excess pore water pressure,  $\Delta u$ , along a vertical profile placed at 1.2 m from P9 pile axis, at different time stations: **a** comparison between reference case  $r01$  and case  $r06$ ; **b** comparison between reference case  $r01$  and case  $r07$

- the thermally induced vertical displacements of the foundation raft (i.e., at the pile heads) can be significant up to a few tens of centimeters in the presence of a higher number of energy piles in the group. This has to be properly taken into account when the assessment of the superstructure serviceability is analyzed;
- the sensitivity study performed on two fundamental thermal properties of the soil has shown that non negligible quantitative differences in foundation loads and excess pore water pressures in the soil might be observed when thermal expansion coefficient and thermal conductivity of the soil vary within the range

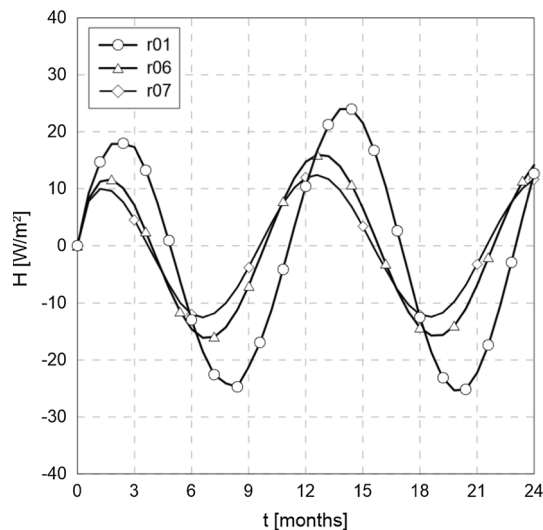


**Fig. 31** Time evolution of the specific heat flux,  $H$ , across the thermo-active pile lateral surface

of values considered. This result indicates that a proper thermal characterization of the soil during the site investigation campaign is of great importance for an accurate prediction of the THM effects on the soil and the foundation structure;

- as far as the thermal efficiency of the system is concerned, the results obtained show that significant thermal interaction effects between the various heat exchangers may occur for closely spaced thermally active piles, even in the case of cyclic (seasonal) heating and cooling. In such conditions, the power input/output of the energy pile system could be much less than proportional to the number of thermally active piles installed per unit area.

The assumption of isotropic elastic soil response adopted in this work cannot be considered as fully appropriate under all possible circumstances, particularly in presence of soft fine-grained soils, and a quite different pattern of foundation loads, soil deformations and excess pore pressures could be obtained if the soil experiences significant (contractant or dilatant) plastic strains.

**Acknowledgements** The financial support of the Project “TIAR–Edilizia Rurale Innovativa Sostenibile con Autonomia Energetica”, funded by the Italian “Ministero delle Politiche Agricole Alimentari e Forestali” is gratefully acknowledged. The Authors wish to thank Ms. Francesca Brunori for the support provided in performing part of the numerical simulations program.

## References

1. Adam D, Markiewicz R (2009) Energy from earth-coupled structures, foundations, tunnels and sewers. *Géotechnique* 59(3):229–236
2. Akrouh GA, Sánchez M, Briaud JL (2014) Thermo-mechanical behavior of energy piles in high plasticity clays. *Acta Geotech* 9(3):399–412
3. Ascher UM, Petzold LR (1998) Computer methods for ordinary differential equations and differential-algebraic equations. Siam, Philadelphia
4. Baldi G, Hueckel T, Pellegrini R (1988) Thermal volume changes of mineral-water system in low porosity clay soils. *Can Geotech J* 25(4):807–825
5. Batini N, Rotta Loria AF, Conti P, Testi D, Grassi W, Laloui L (2015) Energy and geotechnical behaviour of energy piles for different design solutions. *Appl Therm Eng* 86:199–213
6. Bodas Freitas T, Cruz Silva F, Bourne-Webb P (2013) The response of energy foundations under thermo-mechanical loading. In: Proceedings of 18th international conference on soil mechanics and geotechnical engineering, pp 3347–3350
7. Bourne-Webb P, Amatya B, Soga K, Amis T, Davidson C, Payne P (2009) Energy pile test at lambeth college, london: geotechnical and thermodynamic aspects of pile response to heat cycles. *Géotechnique* 59(3):237–248
8. Bourne-Webb P, Bodas Freitas T, Freitas Assunção R (2015) Soil–pile thermal interactions in energy foundations. *Géotechnique* 66(2):167–171
9. Brandl H (2006) Energy foundations and other thermo-active ground structures. *Géotechnique* 56(2):81–122
10. Burghignoli A, Desideri A, Miliziano S (2000) A laboratory study on the thermomechanical behaviour of clayey soils. *Can Geotech J* 37:764–780
11. Campanella RG, Mitchell JK (1968) Influence of temperature variations on soil behavior. *J Soil Mech Found Div ASCE* 94(SM3):709–734
12. Cekerevac C, Laloui L (2004) Experimental study of thermal effects on the mechanical behaviour of a clay. *Int J Numer Anal Methods Geomech* 28(3):209–228
13. Comsol (2014) COMSOL Multiphysics version 4.4: user’s guide and reference manual. Comsol, Burlington
14. Di Donna A, Laloui L (2015) Numerical analysis of the geotechnical behaviour of energy piles. *Int J Numer Anal Methods Geomech* 39(8):861–888
15. Di Donna A, Loria AFR, Laloui L (2016) Numerical study of the response of a group of energy piles under different combinations of thermo-mechanical loads. *Comput Geotech* 72:126–142
16. Dickson MH, Fanelli M (2004) Cos’è l’energia geotermica? Istituto di Geoscienze e Georisorse, CNR, Pisa, pp 8–16
17. Goode J III, McCartney JS (2015) Centrifuge modeling of boundary restraint effects in energy foundations. *J Geotech Geoenviron Eng* 141(8):04015034
18. Heard HC (1960) Transition from brittle failure to ductile flow in Solnhofen limestone as a function of temperature, confining pressure and interstitial fluid pressure. In: Griggs J, Handin JE (eds) Rock deformation, vol 79. The Geological Society of America, Memoir, pp 193–226
19. Hueckel T, Baldi G (1990) Thermoplasticity of saturated clays: experimental constitutive study. *J Geotech Eng ASCE* 116(12):1778–1796
20. Hueckel T, Pellegrini R (1992) Effective stress and water pressure in saturated clays during heating–cooling cycles. *Can Geotech J* 29:1095–1102
21. Jeong S, Lim H, Lee JK, Kim J (2014) Thermally induced mechanical response of energy piles in axially loaded pile groups. *Appl Therm Eng* 71(1):608–615
22. Johnston I, Narsilio G, Colls S (2011) Emerging geothermal energy technologies. *KSCE J Civ Eng* 15(4):643–653
23. Katzenbach R, Ramm H, Waberseck T (2009) Recent developments in foundation and geothermal engineering. In: 2nd

- international conference on new developments in soils mechanics and geotechnical engineering, pp 18–30
24. Laloui L, Di Donna A (2013) Energy geostructures: innovation in underground engineering. Wiley, New Jersey
  25. Laloui L, Nuth M, Vulliet L (2006) Experimental and numerical investigations of the behaviour of a heat exchanger pile. *Int J Numer Anal Methods Geomech* 30(8):763–781
  26. Lewis RW, Schrefler BA (1998) The finite element method in the deformation and consolidation of porous media, 2nd edn. Wiley, New Jersey
  27. Mimouni T, Laloui L (2015) Behaviour of a group of energy piles. *Can Geotech J* 52(12):1913–1929
  28. Mitchell JK, Soga K (2005) Fundamentals of soil behavior, 3rd edn. Wiley, New Jersey
  29. Murphy K, McCartney JS (2014) Seasonal response of energy foundations during building operation. *Geotech Geol Eng* 33(2):343–356
  30. Murphy KD, McCartney JS, Henry KS (2015) Evaluation of thermo-mechanical and thermal behavior of full-scale energy foundations. *Acta Geotech* 10(2):179–195
  31. Ng CWW, Shi C, Gunawan A, Laloui L (2014) Centrifuge modelling of energy piles subjected to heating and cooling cycles in clay. *Geotech Lett* 4(4):310–315
  32. Nova R, Castellanza R, Tamagnini C (2004) A constitutive model for mechanical and thermal loading of bonded geomaterials based on the concept of plasticity with extended hardening. In: Proceedings of 9th symposium on numerical models in geomechanics (NUMOG IX), pp 51–56
  33. Olgun C, Abdelaziz S, Martin J (2012) Long-term performance and sustainable operation of energy piles. In: Proceedings of ICSDDEC 2012: developing the frontier of sustainable design, engineering, and construction, ASCE Reston, VA, pp 534–542
  34. Rotta Loria AF, Laloui L (2016) Thermally induced group effects among energy piles. *Géotechnique* 67(5):374–393
  35. Salciarini D, Ronchi F, Cattoni E, Tamagnini C (2013) Thermomechanical effects induced by energy piles operation in a small piled raft. *Int J Geomech* 15(2):04014,042
  36. Stewart MA, McCartney JS (2014) Centrifuge modeling of soil-structure interaction in energy foundations. *J Geotech Geoenviron Eng* 140(4):04013,044
  37. Suryatriyastuti M, Burlon S, Mroueh H (2016) On the understanding of cyclic interaction mechanisms in an energy pile group. *Int J Numer Anal Methods Geomech* 40(1):3–24
  38. Wang W, Regueiro RA, Stewart M, McCartney JS (2012) Coupled thermo-poro-mechanical finite element analysis of an energy foundation centrifuge experiment in saturated silt. In: GeoCongress 2012, American Society of Civil Engineers, pp 4406–4415
  39. Wang W, Regueiro RA, McCartney JS (2015) Coupled axisymmetric thermo-poro-mechanical finite element analysis of energy foundation centrifuge experiments in partially saturated silt. *Geotechn Geol Eng* 33(2):373–388
  40. You S, Cheng X, Guo H, Yao Z (2016) Experimental study on structural response of cfg energy piles. *Appl Therm Eng* 96:640–651